International Journal of Biological Macromolecules 289 (2025) 138657

Contents lists available at ScienceDirect

International Journal of Biological Macromolecules

journal homepage: www.elsevier.com/locate/ijbiomac

Comparison on the performance of green and conventional magnetic chitosan-based composites in the removal of complex dyes: Synergetic effect, experimental and theoretical studies

Natália Gabriele Camparotto [a], Gabriel Henrique Silva Fulaneti [a], Harold Hilarion Fokoue [a], Valmor Roberto Mastelaro [b], Melissa Gurgel Adeodato Vieira [c], Patrícia Prediger [a,*]

[a] School of Technology, University of Campinas – UNICAMP, 13484-332 Limeira, São Paulo, Brazil
[b] São Carlos Institute of Physics, University of São Paulo – USP, 13566-590 São Carlos, São Paulo, Brazil
[c] School of Chemical Engineering, University of Campinas – UNICAMP, 13083-852 Campinas, São Paulo, Brazil

ARTICLE INFO

Keywords:
Green synthesis
Adsorption
Dyes
Iron nanoparticles
Chitosan

ABSTRACT

The presence of complex dyes, which possess four or more aromatic rings, is pervasive in environmental matrices. Nanomaterials offer a promising avenue for their removal. In this study, we synthesized novel magnetic nanocomposites comprising nanochitosan (nCS) and iron nanoparticles through the application of green and conventional protocols. In the preparation of the green composite, designated as G-nCS@FeNPs, eucalyptus leaves extract and proanthocyanidins were employed as reducing and crosslinking agents, respectively. In contrast, the conventional composite, designated as C-nCS@FeNPs, utilized ammonia and glutaraldehyde as the reducing and crosslinking agents, respectively. The G-nCS@FeNPs exhibited a more electropositive surface, and prominent magnetic properties. The zeta potential measurements of the G-nCS@FeNPs (ranging from +36 to +30 mV) were more positive than those of the C-nCS@FeNPs (+35 to −2.79 mV). Additionally, the C content in C-nCS@FeNPs was less (36.4 %) than in G-nCS@FeNPs (57.2 %), which is likely due to the higher nanochitosan content and the presence of proanthocyanidins in the green nanocomposite. The G-nCS@FeNPs exhibited a tridimensional porous structure, whereas the conventional composite appeared to form a CS film with an uneven surface and embedded FeNPs. G-nCS@FeNPs demonstrated remarkable potential as an adsorbent material for the removal of anionic reactive dyes, namely orange 122 (RO122) and red 250 (RR250). It exhibited an exceptional adsorption capacity of 3005 $mg.g^{-1}$ for RO122. A DFT study revealed that the RO122 molecule displays enhanced reactivity towards the adsorbent surface. Moreover, experiments conducted in saline media and XPS and FTIR analyses post-adsorption indicated that 78.8 % of the interactions between RO122 and the adsorbent are based on electrostatic and ion exchange, while the remaining 22.2 % are attributed to π-π and hydrogen bonds. Also, G-nCS@FeNPs demonstrated a synergistic effect on the removal of the cationic dye safranin in multicomponent systems, exhibiting an increase in removal capacity from 0 to 169 $mg.g^{-1}$.

1. Introduction

The discharge of domestic waste and effluent into water bodies represents a significant ecological problem on a global scale, with significant implications for the sustainability of aquatic ecosystems. The utilization of dyes many industrial activities has been identified as a significant contributor to the contamination of water sources [1]. Dyes are an indispensable component in industries, including textiles, food, leather, and paper. It is estimated that over 100,000 distinct types of dyes, amounting to approximately one million tons, are produced annually [2]. A considerable quantity of wastewater generated by these industries is discharged into rivers, lakes, and oceans without any treatment. Approximately 20 % of the dyes present in this wastewater are not removed [3].

The presence of dyes in water can impede the photosynthetic activity of aquatic plants by obstructing the penetration of sunlight and oxygen, which may inhibit the optimal growth of aquatic life. Moreover, it is crucial to acknowledge that a significant portion of dyes are not

* Corresponding author.
E-mail address: prediger@unicamp.br (P. Prediger).

https://doi.org/10.1016/j.ijbiomac.2024.138657
Received 14 August 2024; Received in revised form 26 November 2024; Accepted 9 December 2024
Available online 11 December 2024

biodegradable and can persist in the environment due to their complex aromatic structures [2,4]. Many dyes are toxic to biodiversity and human health [5]. Anionic dyes are considered complex structures due to their four or more aromatic rings, which confer resistance to degradation [6]. Fig. 1 depicts the complex chemical structures of two anionic dyes: reactive red 250 (RR250) and reactive orange 122 (RO122).

Several conventional methods have been developed to eliminate dyes. These include biological methods (bacterial, fungal, and yeast biodegradation) [3], physical methods (flocculation, coagulation, ultrafiltration, ion exchange, membrane separation), and chemical methods (oxidation, catalysis, photolysis, chemical precipitation, ozonation, electrolysis, and UV irradiation) [1,2]. Oxidation is an effective method for the degradation of a range of dyes and other recalcitrant compounds. However, it has the inherent limitation of forming toxic by-products and requires strict control of operating conditions [7,8]. Membrane separation also exhibits high efficiency in the removal of dyes; however, it is prone to clogging, necessitating frequent cleaning. Furthermore, its efficacy is limited for smaller molecules [9]. In general, these treatments are incapable of completely removing dyes from water and wastewater, and they are not environmentally friendly [2].

Nanomaterials have the potential to remove organic dyes from the environment through adsorption due to their high surface area and pore volume. The adsorption process is a relatively simple method whereby the molecules of the pollutant are retained on the surface of the nanomaterial through physical and/or chemical interactions. [10,11]. However, most nanomaterial synthesis processes employ the use of harmful chemicals, including organic solvents, strong acids or bases, and oxidizing or reducing agents. The use of these chemicals inevitably results in the generation of toxic byproducts and waste [12]. Consequently, current research describes the synthesis of eco-friendly nanomaterials by substituting harmful chemicals with biological sources [13–15].

Chitosan (CS) is a biopolymer derived from chitin that is primarily found in the exoskeletons of crustaceans, including shrimp, crabs, and insects. CS is regarded as a biocompatible, environmentally friendly, and biodegradable material with antibacterial properties [16]. This material displays advantageous characteristics that render it an optimal candidate for water treatment [17]. The high adsorption potential, abundance, and low cost of this material render it an attractive option. The molecular structure of CS contains amino and hydroxyl groups, which serve as active sites for the sorption of contaminants [17,18]. Several studies have demonstrated the ability of CS to be configured into a variety of forms, including gels, membranes, beads, microparticles, nanoparticles, and sponges. Among these, chitosan nanoparticles (CSNPs) are distinguished as an adsorbent material with a high potential for a novel and efficacious water and wastewater decontamination process [16,18].

CSNPs can be combined with other particles to create new composites with enhanced properties, which improve the adsorption potential. He et al. (2023) immobilized the cellulose-chitosan composite in aerogels and applied them to remove methyl orange dye. The authors reported that the generation of the composite resulted in excellent structural stability of the material, and the chemical groups present in both materials facilitated dye removal [19]. One strategy to enhance adsorption and facilitate the removal of the substance from the medium after the process is to insert iron nanoparticles (FeNPs). The preparation of FeNPs can be achieved through the utilization of either traditional or green chemistry-based methodologies. Conventional methodologies rely on the use of toxic reducing agents, such as sodium borohydride and ammonia. In contrast, green protocols employ a range of natural resources, including plants, fungi, and waste materials, to generate nanoparticles.

The formation of composites comprising disparate particles requires the use of a crosslinking agent. Commonly employed agents include glutaraldehyde (GLUT) and epichlorohydrin, which are toxic compounds [20]. Proanthocyanidins (PAS) are formed by oligomers and polymers bound to the flavan-3-ol framework and can be found in several plants' fruits and flowers. They are promising non-toxic and natural crosslinking agents [15,21].

Numerous studies have been conducted on the synthesis and application of ecological composites. However, few studies have conducted a comprehensive and objective comparison of the morphological and chemical characteristics, as well as the adsorption performance, of eco-friendly composites in comparison to conventionally prepared composites. In this study, we synthesized novel magnetic composites with CS and iron nanoparticles using both green and conventional protocols and conducted a comparative analysis of their chemical and morphological characteristics, as well as their adsorption efficiency for toxic complex dyes. The conventional protocol employed ammonia and glutaraldehyde, whereas the green protocol utilized eucalyptus leaf extract and proanthocyanidins, which served as reducing and crosslinking agents, respectively. The composites were subjected to characterization using X-ray diffraction (XRD), Fourier-transform infrared spectroscopy (FTIR), scanning electron microscopy (SEM), vibrating sample magnetometer (VSM), and zeta potential analysis. The nanocomposites were applied to remove reactive red 250 (RR250), reactive orange 122 (RO122), and safranin (SF). The study evaluated the effectiveness of adsorption in relation to pH, contact time, and adsorbent dosage. Kinetic, isothermal, and thermodynamic studies were conducted in order to gain further insight into the underlying mechanisms. A Density Functional Theory (DFT) study was conducted to evaluate the molecular descriptors associated with the complex dyes, with the objective of gaining a deeper understanding of the adsorption system at the molecular level. To assess the adsorption capacity of the nCS@FeNPs composite in the presence of interfering agents, a real river water sample was employed. To the best of our knowledge, this is the inaugural study to contrast the synthesis of magnetic CS-based composite via green and conventional protocols, with an emphasis on their characteristics and efficacy in dye adsorption.

2. Materials and methods

2.1. Materials

Oleic acid (89,5 %), ethyl alcohol (98 %), safranin (SF, 95 %), sodium tripolyphosphate (TPP, 95 %), iron chloride II (99 %), and III (98 %) were purchased from Dinâmica (Indaiatuba, SP, Brazil). Sodium hydroxide (NaOH, 98 %), ammonia hydroxide (NH_4OH, 98 %; 51.94 %

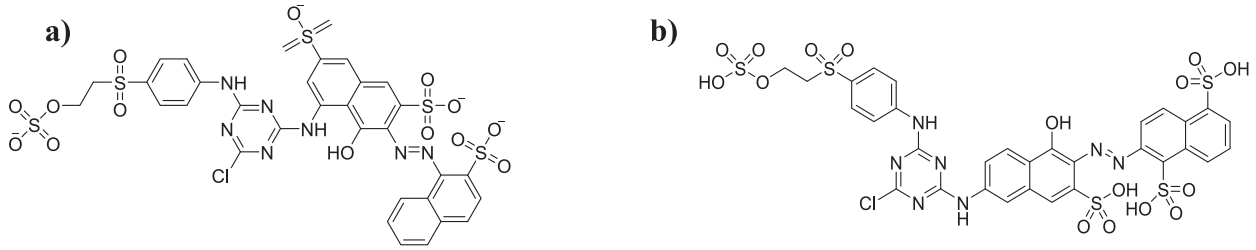

Fig. 1. Chemical structure of the dyes (a) RR250; (b) RO122.

of NH_3 in weight), chloride acid (HCl, 98 %), acetone (98 %), and glacial acetic acid (high purity, 99.7 %) were acquired from Synth (Diadema, SP, Brazil). Chitosan (low molecular weight, <100,000 $g.mol^{-1}$) and glutaraldehyde solution (Grade II, 25 % v/v) were purchased from Sigma Aldrich (Milwaukee, WI, USA). Proanthocyanidin (PAS) was purchased from Galena Farmacêutica (Campinas, SP, Brazil). Eucalyptus extract (*Eucalyptus globulus Labill*) was acquired from UNICAMP (Limeira, SP, Brazil). Reactive orange 122 (RO122), and reactive red 250 (RR250) were purchased from Danny Color Comércio de Corantes Ltda (São Paulo, SP, Brazil).

2.2. Conventional synthesis of iron nanoparticles

Conventional iron nanoparticles (C-FeNPs) were synthesized based to the methodology proposed by Silva et al. (2013) [22]. In a 250 mL round-bottom reaction flask, 10 mL of iron chloride II and III and 0.5 mL of oleic acid were vigorously stirred at 1400 rpm. Subsequently, NH_4OH was added dropwise until the system reached a pH of 11. The reaction was conducted at a temperature of 85 °C for 30 min. The system was then filtered and washed with ultrapure water until the pH reached 7. The resulting precipitate was then dried in a Lucadema heating oven for three days at 40 °C and subsequently stored at room temperature.

2.3. Green synthesis of iron nanoparticles

The synthesis of green iron nanoparticles (G-FeNPs) followed the methodology proposed by Zhang et al. (2021), with modifications [23]. Eucalyptus leaves were collected, washed with ultrapure water, and air-dried for a period of 24 h. Subsequently, the dried leaves pulverized, and the resulting powder (10 g) was added to 150 mL of water at 80 °C. The system was then heated for 1 h, and the extract was filtered. Iron chloride III and iron chloride II were added to a 2 L beaker in a 2:1 ratio. Then, 17 mL of eucalyptus extract and 1.5 mL of oleic acid were added to the mixture. The reaction underwent vigorous mechanical stirring at room temperature, and a 1 M NaOH solution was added dropwise until the system's pH reached 7. The reaction was then heated to 55 °C and kept under vigorous stirring for 1 h. Aqueous NaOH solution (1 M) was added to the mixture while heating until the pH of the medium reached 11. The reaction medium was stirred for another 30 min while heating. The mixture was filtered using a Büchner funnel and ultrapure water until the pH reached 7. The retained material was then dried in an oven at 40 °C for 48 h.

2.4. Synthesis of chitosan nanoparticles

Chitosan nanoparticles (CSNPs) were prepared with modifications based on the methodology proposed by Pereira et al. (2017) [24]. Initially, 1 g of CS (with 88 % of deacetylation degree [25]) was dissolved in acetic solution (2 % *v*/v) and kept under magnetic stirring overnight at 600 rpm. Then, a sodium tripolyphosphate (TPP) solution (5 % v/v) was prepared and stirred until complete dissolution. Using a peristaltic pump, the TPP solution was slowly dripped into the stirring CS solution (1000 rpm).

2.5. Preparation of magnetic composites nCS@FeNPs

2.5.1. Conventional nCS@FeNPs magnetic composite

A mixture of 1 L of ultrapure water, 1 g of nCS, and 1 g of C-FeNPs was sonicated for 1 h in a beaker flask. Then, 3.77 mL of the crosslinking agent glutaraldehyde (GLUT, 37 wt% solution in H_2O) was added, and the system was stirred for 1 h at 1200 rpm. Finally, the crude reaction product was washed and filtered with ultrapure water (1 L) in a Büchner funnel and stored in suspension in an amber flask. The generated material (C-nCS@FeNPS) was purified using a magnetic magnet.

2.5.2. Green nCS@FeNPs magnetic composite

A mixture of 1 L of ultrapure water, 1 g of nCS, and 1 g of G-FeNPs was sonicated for 1 h in a beaker flask. Afterward, 1 g of the crosslinking agent proanthocyanidin (PAS) was added, and the system was stirred for 1 h at 1200 rpm. Finally, the crude reaction product was washed and filtered with ultrapure water (1 L) in a Büchner funnel and stored in suspension in an amber flask. The generated material (G-nCS@FeNPS) was purified using a magnetic magnet.

A scheme of the preparation of the composites is presented in Fig. 2.

2.6. Characterizations

The crystalline structure was analyzed using Shimadzu XRD7000 equipment at 25 °C. Cu K-α radiation with λ = 1.54 nm was used at 40 kV and 30 mA. Prior to measurement, the samples were dried in an oven at 40 °C for 12 h. The Debye-Scherrer equation (Eq. 1) was applied to obtain the particles size of FeNPs.

$$D = \frac{K.\lambda}{\beta.\cos\theta} \quad (1)$$

where: D = size (nm); K = Debye-Scherrer constant (0.89), λ = wavelength used in the equipment (0.15406 nm); β = the maximum peak width at half height and θ = the diffraction angle.

The functional groups were analyzed using Agilent FTIR-Cart 630 spectrometric equipment with the KBr pellet method. The equipment scanned from 4000 to 400 cm^{-1}. X-ray Photoelectron Spectroscopy (XPS) analyses were conducted using a Scienta Omicron ESCA+ spectrometer equipped with an EAC2000 hemisphere analysis system. Monochromatic radiation A1 Kα with a photon energy (h ν) of 1486.6 eV was used as the electronic excitation source. To avoid surface charge effects, a CN10 charge neutralizer was utilized. High resolution XPS spectra were obtained with a constant pass energy of 30 eV and a step size of 0.05 eV. The binding energies were referenced to the C 1 s peak at 284.8 eV. Data analysis was performed using CasaXPS software. Structural and morphological characteristics were analyzed using scanning electron microscopy (SEM) with Tescan equipment Vega 3 SEM. C-FeNPs and G-FeNPs were affixed to the sample holder using double-sided carbon adhesive, while nCS, C-nCS@FeNPs, and G-nCS@FeNPs were deposited on a silicon plate affixed to the sample holder with double-sided carbon adhesive and then coated with an ultra-thin gold film using vacuum spraying. The magnetization at room temperature was measured using a vibrating sample magnetometer (VSM). The surface charge was analyzed using a Zetasizer Nano ZS (Malvern) at pH values ranging from 4 to 10, with a concentration of 0.01 mg/mL. The pH was adjusted by adding HCl or NaOH solutions. Prior to measurement, the C-FeNPs and G-FeNPs samples were magnetically shaken for 24 h.

2.7. Adsorption study in ultrapure water, river water and saline media

Batch adsorption experiments were conducted to describe the adsorption of contaminants by the composites. The efficiency parameters used were the adsorption capacity (Eq. 2, qe) and removal efficiency (Eq. 3, Removal %).

$$qe = \frac{(Ci - Cf).V}{Mads} \quad (2)$$

$$Removal\% = \frac{Ci - Cf}{Ci} \quad (3)$$

where qe ($mg.g^{-1}$) is the adsorption capacity; C_i ($mg.L^{-1}$) is the initial concentration; C_f ($mg.L^{-1}$) is the final concentration; V (L) is the volume of the solution; and M_{ads} (g) is the mass of adsorbent material.

The effect of the parameters was assessed by altering the pH within the range of 2 to 12 from the addition of NaOH and HCl (1 M), contact

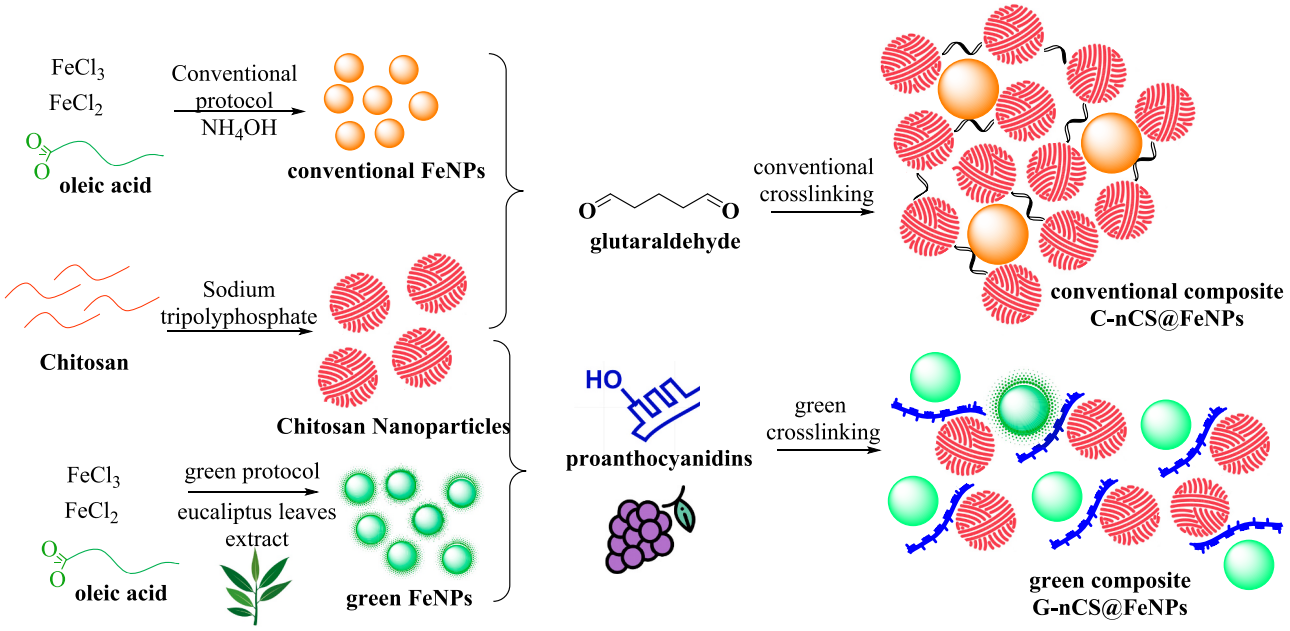

Fig. 2. Scheme of the preparation of C-nCS@FeNPs and G-nCS@FeNPs.

time (between 0.5 and 300 min), adsorbent concentration (between 0.2 and 1 g.L^{-1}), dye concentration (between 50 and 700 mg.L^{-1}) and temperature (298, 308 and 328 K).

The samples underwent analysis using a UV–vis spectrophotometer (FEMTO 700) at wavelengths of 486 nm, 545 nm, and 520 nm for RO122, RR250, and SF, respectively. After each experiment, the adsorbent was removed from the solution using a magnet and disposed of in suitable packaging.

Adsorption tests were conducted on a sample collected from the Ribeirão do Pinhal River (São Paulo, Brazil) and enriched with 5 mg.L^{-1} of the RO122 dye.

The adsorption test of the RO122 dye in multicomponent systems was evaluated in the presence of the anionic dye RR250 and the cationic dye SF.

The experiments in saline media were carried out with NaCl concentration of 100 mg.L^{-1}. The concentration of RO122 and RR250 dyes was 100 mg.L^{-1}.

The Supplementary Material presents the calculations for the kinetic, isothermal, and thermodynamic studies.

2.8. Molecular modeling

Molecular modeling was conducted via density functional theory (DFT) calculations. The Avogadro 1.2.0 software was employed as the interface to generate the three-dimensional chemical structures of the RO122 and RR250 dyes. The highest energy occupied molecular orbital (HOMO, EH) and the lowest energy unoccupied molecular orbital (LUMO, EL) were calculated using Orca software, version 4.2.3, from the B3LYP theory and the DEF2-SVP basis set. The quantum-chemical descriptors, including the overall chemical hardness (η), the electronic chemical potential (μ), and the overall electrophilicity index (ω), were calculated from the HOMO and LUMO values obtained using eqs. 4, 5, and 6.

$$\mu = -(E_H + E_L)/2 \quad (4)$$

$$\eta = (-E_H + E_L)/2 \quad (5)$$

$$\omega = \mu^2/2\eta \quad (6)$$

3. Results and discussion

3.1. Adsorbent characterizations

3.1.1. Physical analyses

The XRD patterns of C-FeNPs, G-FeNPs, nCS, and composites are shown in Fig. 3. In the XRD pattern of C-FeNPs (black line) e G-FeNPs (red line), characteristic peaks around 35.6°, 43.4°, 57.2° e 62.9° correspond to the crystalline planes (311), (400), (511) and (440), respectively, indicating the presence of cubic magnetite nanoparticles [15,26]. The Debye-Scherrer equation was employed to determine the dimensions of the synthesized particles. The particle size of C-FeNPs was determined to be 12.7 nm, whereas that of G-FeNPs was found to be 14.2 nm, thereby confirming the synthesis of particles on a nanoscale. Appu et al. (2021) [27] also yielded comparable results. The researchers prepared iron nanoparticles using leaf extracts of *Brassica oleracea*, and the resulting particle size, using the Debye-Scherrer equation, was found to be 14 nm.

In the XRD pattern of nCS (Fig. 3, blue line), characteristic peaks were observed at 20.4° and 22.8°, 26.5°, 33.2° e 38.8°, indicating high

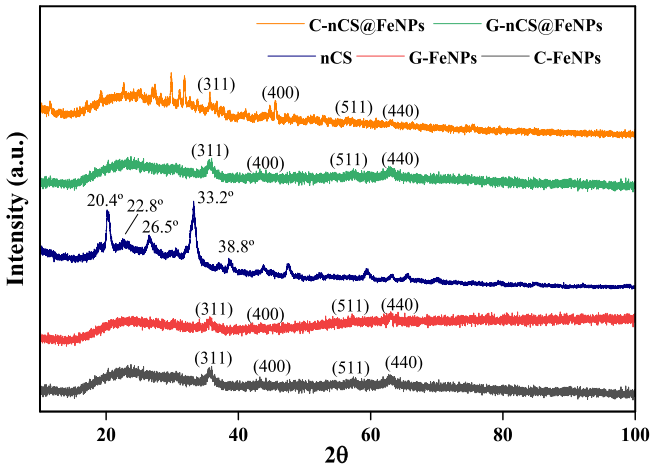

Fig. 3. XRD patterns of C-FeNPs (black line), G-FeNPs (red line), nCS (blue line), G-nCS@FeNPs (green line), and C-nCS@FeNPs (orange line).

crystallinity due to the presence of the crosslinking agent TPP [28], confirming the formation of CS nanoparticles. Alehosseini et al. (2022) reported high crystallinity of chitosan nanoparticles due to ionic interactions between CS and TPP [29], confirming similar findings. The XRD pattern of the G-nCS@FeNPs (green line) exhibited the presence of peaks associated with FeNPs and CS. The peaks related to CS were more discernible in the G-nCS@FeNPs, suggesting a major CS content in this composite. The C-nCS@FeNPs XRD pattern (orange line) revealed the presence of CS and FeNPs, indicating successful generation of the composite.

To confirm and evaluate the morphological characteristics of the pure materials (C-FeNPs, and G-FeNPs) and the composites (C-nCS@FeNPs and G-nCS@FeNPs) SEM analyses were performed (Fig. 3). To conduct the SEM analyses, the material suspensions were subjected to drying, which resulted in the agglomeration of nanoparticles due to van der Waals interactions between Fe_3O_4 nanoparticles [26], forming blocks with a diameter of approximately 20 μm. Biswas et al. (2024) obtained SEM images of iron nanoparticles, which revealed that the material formed shapeless agglomerates measuring 10 μm [30].

Regarding C-FeNPs (Fig. 4 a-c), this material showed the smallest particle size in comparison to the G-FeNPs (Fig. 4 d-f). Queiroz et al. reported the formation of Fe_3O_4 nanoparticles agglomerates synthesized through green and conventional routes [15]. The green Fe_3O_4 agglomerates were observed to have a larger size compared to the conventionally prepared nanoparticles.

Following the composite formation, the visibility of nCS and FeNPs in the morphology of C-nCS@FeNPs (Fig. 4 g-i) and G-nCS@FeNPs (Fig. 4 j-l) diminished, suggesting agglomeration between the two materials, likely due to the crosslinking agents employed. A change in the surface of the composite compared to pure nanoparticles was also reported by Cheng et al. (2024), who synthesized a magnetic composite of biochar with chitosan. The authors observed a change in the surface of the material, with the apparent magnetic nanoparticles becoming undetectable [31].

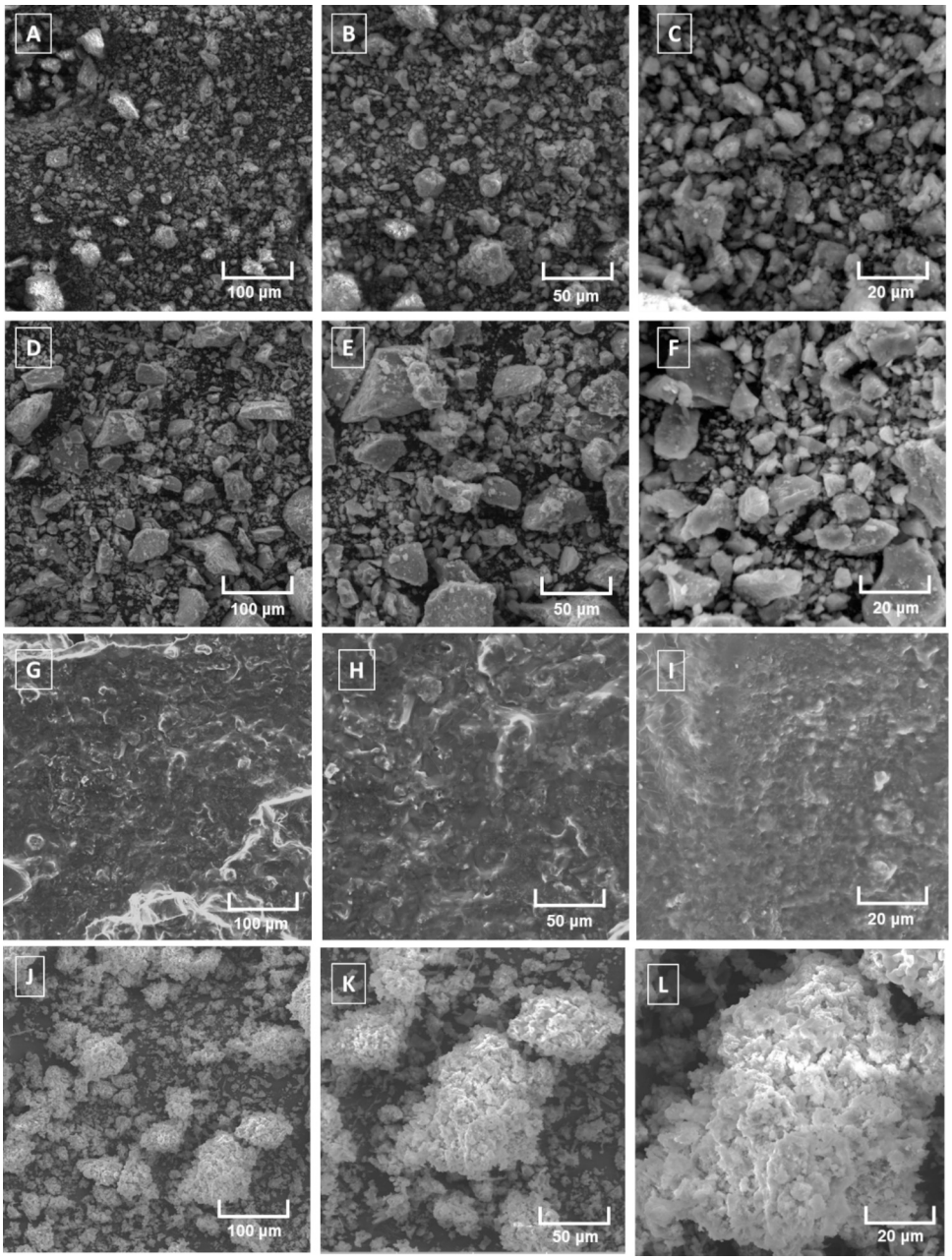

Fig. 4. SEM images of **(a-c)** C-FeNPs; **(d-f)** G-FeNPs; **(g-i)** C-nCS@FeNPs; and **(j-l)** G-nCS@FeNPs.

The SEM images of C-nCS@FeNPs suggest the formation of a CS film, with an uneven surface, containing the iron nanoparticles (Fig. 4 g-i). Similarly, Neves et al. (2020) [26] documented the formation of a CS film comprising magnetic Fe_3O_4 nanoparticles cross-linked with glutaraldehyde, employing the identical conditions utilized in the conventional synthesis methodology presented in this study. Conversely, the SEM images of G-nCS@FeNPs revealed the formation of a three-dimensional porous material, which underscores the significant impact of the methodologies on the material properties. (Fig. 4 j-l). The findings indicate that the incorporation of proanthocyanidins as a cross-linking agent has imparted augmented characteristics to the composite. In addition to using naturally occurring and non-toxic compounds, this approach offers a promising avenue for enhancing the composite's properties.

3.1.2. Chemical analyses

The surface charge of the materials was analyzed using zeta potential at different pH (4, 6, 8, and 10). The results are presented in Fig. 5a. The nCS suspensions exhibited positive surface charges ranging from +36 mV to +29, which can be attributed to the presence of protonated amine groups [32]. The net zeta potential is observed to decrease when negatively charged TPP reacts with positively charged chitosan. Consequently, an elevated zeta potential corresponds to a diminished TPP proportion within the nanoparticle. Yu et al. (2013) obtained similar zeta values for CS nanoparticles cross-linked with TPP [33].

The surface charge of the G-nCS@FeNPs composite showed a similar profile to that of nCS, with zeta potential values ranging from +36 to +30 mV. This profile may be associated with the presence of nCS, Fe^{2+}, and Fe^{3+} in the composite. As indicated by XRD data (Fig. 3), the CS content appears to be higher in the green composite than in the conventionally prepared one. This may result in a markedly enhanced positive charge in the green composite. Appu et al. (2021) also found that a composite based on CS and Fe_3O_4 nanoparticles, prepared from a green route with leaf extracts of *Brassica oleracea L.,* exhibited a positive zeta potential, reaching +76.9 mV [27].

In contrast, the zeta potential of C-nCS@FeNPs decreased from +35 to −2.79 mV as the pH increased from 4 to 10, indicative of the emergence of a more electronegative material at basic pH compared to the green material. In a previous study, Peralta et al. (2019) [34] demonstrated that a magnetic composite formed by CS and Fe_3O_4 nanoparticles prepared via a conventional route exhibited comparable zeta potential values, ranging from +35 to −10 mV. In their study, Munim et al. (2020) [35] observed that the composite formed by CS and nanocellulose exhibited a positive surface charge until the pH reached 7. After this point, the surface charge was approximately −20 mV.

As evidenced by the XRD analysis (Fig. 3), the presence of nCS on the

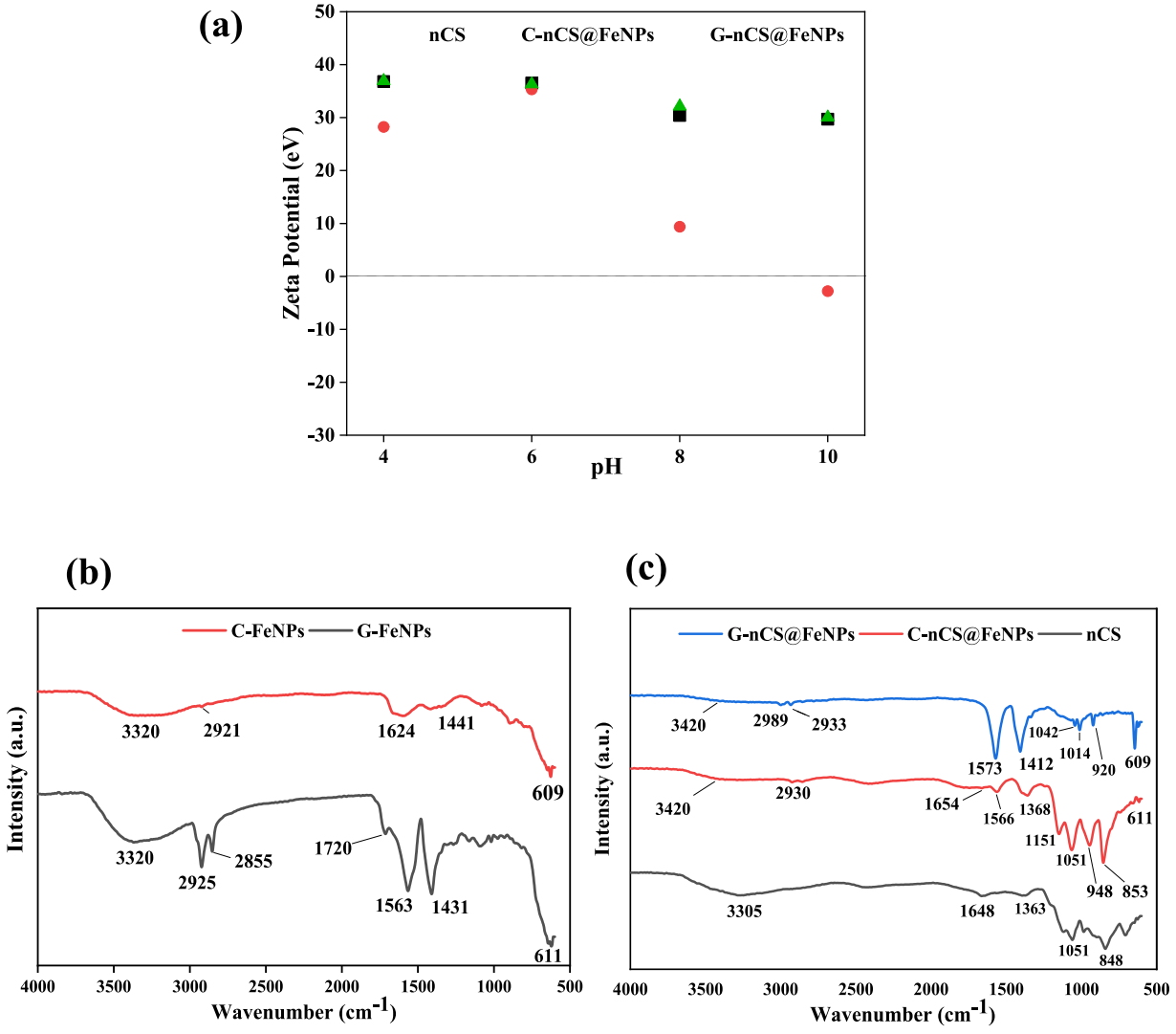

Fig. 5. (a) Zeta potentials of suspensions of nCS, C-nCS@FeNPs and G-nCS@FeNPs; (b) FTIR spectrum of C-FeNPs (red line) and G-FeNPs (black line); (c) FTIR spectrum of nCS (black line) and composites C-nCS@FeNPs (red line) and G-nCS@FeNPs (blue line).

surface of the C-nCS@FeNPs composite could not be discerned, indicating that PAS exerted a more pronounced influence on the crosslinking between nCS and G-FeNPs. In light of these findings, it can be posited that G-nCS@FeNPs displays the greatest potential for the removal of anionic dyes [15].

Fig. 5a-b displays the FTIR spectra of the synthesized iron nanoparticles and composites. The G-FeNPs spectrum showed more intense bands compared to the conventionally prepared FeNPs. The spectra of C-FeNPs (red line) and G-FeNPs (black line) (Fig. 5b) showed a broad band at 3320 cm^{-1}, corresponding to the O—H stretching vibration. The stretching vibrations of the $–CH_2$ groups of aliphatic hydrocarbons are attributed to the bands at 2921, 2925, and 2855 cm^{-1}, confirming the presence of oleic acid in the NPs generated [36]. In C-FeNPs the band at 1441 cm^{-1} is related to the $–CH_3$ groups and in the G-FeNPs the band at 1431 cm^{-1} is assigned to symmetrical bending in the plane of C—H bond, as observed in the FTIR spectrum of eucalyptus extract [37]. Regarding the bands attributed to phenolic compounds in the eucalyptus extract, it is worth noting that the bands at 1720 and 1563 cm^{-1} are a result of the presence of C═O groups and aromatic rings [38]. In the FTIR spectrum of C-FeNPs, the band at 1624 cm^{-1} is assigned to the asymmetric and symmetric bands (COO^-), due to the presence of oleic acid [39]. The bands at 611 and 609 cm^{-1} may be associated with Fe—O [40], confirming the presence of iron oxide [23]. Furthermore, the band around 600 cm^{-1} can also reveal the formation of cubic magnetite nanoparticles [23].

A large band was observed around 3305 cm^{-1} in the nCS spectrum (black line, Fig. 5c), which can be attributed to the O—H stretching vibration. The band at 1648 cm^{-1} corresponds to the stretching vibration of the C═O groups, indicating the presence of amide [41]. The presence of C−N stretching vibrations is suggested by the band at 1363 cm^{-1} [42]. The 1064 cm^{-1} band is attributed to the presence of C–O–C groups of CS scaffold [43], whereas the 848 cm^{-1} band is due to P═O stretching vibrations resulting from TPP, the crosslinking agent of CS nanoparticles [44].

In the C-nCS@FeNPs spectrum (red line, Fig. 5c), the bands at 3320 and 3305 cm^{-1}, associated with O—H stretching in the FTIR spectra of pure FeNPs and CS, respectively, red-shifted to 3420 cm^{-1}. This shift indicates the presence of interactions between CS and GLUT through hydrogen bonds [45]. The slight band at 1654 cm^{-1} is related to the presence of amide in the CS acetylated rings [46] and the band at 1566 cm^{-1} are attributed to the formation of imine groups (HC=N−) resulting from interactions between the NH_2 groups of CS and the aldehyde groups of the crosslinking agent used in the composite preparation [46,47]. The disappearance of the peak at 1720 cm^{-1} referring to the C═O stretching present in C-FeNPs was noticeable, indicating the reaction between FeNPs and GLUT [48]. The bands at 1151 and 1051 cm^{-1} refer to C–O–C groups of CS scaffold [43,49].

Also, in the G-nCS@FeNPs spectrum (blue line, Fig. 5c), the 3320 and 3305 cm^{-1} bands related to O—H stretching in the FTIR spectra of the pure FeNPs and CS, respectively, red-shifted to 3420 cm^{-1}, indicating interactions between CS and PAS through hydrogen bonds [50]. Similar behavior was observed by Bi et al. (2019) in the formation of CS and PAS films [51]. The bands at 1573 and 1412 cm^{-1} referred to C═C stretching and C−H of the aromatic ring, respectively [51]. The bands at 1042 and 1014 cm^{-1} are related to C–O–C of nCS and PAS [43].

The XPS analyses of the surface of the synthesized FeNPs and composites are shown in Fig. 6 a and Table 1 displays the data obtained from the XPS spectra survey. The nCS exhibited 43.5 % carbon, 37.0 % oxygen, and 1.9 % nitrogen. As a consequence of the crosslinking process between nCS and TPP, the presence of sodium (6.3 %) and phosphorus (11.3 %) was confirmed. The C-FeNPs exhibited a carbon percentage of 63.9 %, which was higher than that observed for the G-FeNPs (37.4 %). Conversely, the G-FeNPs exhibited a higher iron percentage (16.3 %) than the C-FeNPs (3.4 %). This difference may be related to the efficiency of the crosslinking process, suggesting that proanthocyanidins are more effective crosslinking agent. In a similar study, Queiroz and colleagues observed comparable results when preparing green and conventional magnetic composites cross-linked with proanthocyanidins and glutaraldehyde [15]. The composite cross-linked with proanthocyanidins exhibited double the iron content.

Regarding the composites, C-nCS@FeNPs exhibited higher phosphorus (14.0 %) and oxygen (41.8 %) contents than the green composite, what is probably related to the higher content of polyphosphate groups of the CS crosslinking agent. This analysis corroborates the results observed for zeta potential measurements (Fig. 5), in which the conventionally prepared composite exhibited a more negatively charged surface. The G-nCS@FeNPs showed a higher carbon content (57.2 %), probably due to the oleic acid and natural organic compounds from the plant extract used in the material' synthesis. With relation to the iron content, C-nCS@FeNPs exhibited 0.1 %, whereas the green G-nCS@FeNPs composite exhibited 1.0 %. The XPS technique analyzes and quantify the elements present in the material' surface [52], and in the case of composite materials, with an irregular composition, it is reasonable to anticipate discrepancies in the elemental content, given that the FeNPs are heterogeneously distributed in the composite [53]. de Almeida et al. (2022) [54] similarly observed a low iron loading (1.2 %) for a magnetic composite comprising graphene oxide and CS crosslinked with glutaraldehyde.

The high-resolution C1s XPS spectrum of nCS (Fig. 6a) revealed the presence of four components centered at 284.7, 286.1, 287.8 and 288.9 eV, which correspond to C–C/C–H (48.7 %), C–N/C–O (34.2 %), C═O (10.3 %), O–C–O/O–C=O (6.8 %), respectively [55]. Similar composition was observed by Rodrigues et al. (2012) [56]. Regarding nitrogen, the high-resolution N 1 s spectrum (Fig. 6b) showed the presence of two components at 399.2 and 400.8 eV. The first corresponds to C—N bonds (81 %) of CS amines and amides [57] and the second is related to protonated amine group ($-NH_3^+$) (19 %) of CS [58].

The high-resolution C1s XPS spectrum of C-FeNPs (Fig. 6c) revealed the presence of five components centered at 284.7, 285.7, 286.8, 288.2, and 289.5 eV, which correspond to C–C/C–H (50.8 %), C–N/C–O (28.5 %), N–C=O (9.0 %), C═O (7.4 %), O–C–O/O–C=O (4.4 %), respectively [15,26]. In the Fe 2p high-resolution XPS spectrum of C-FeNPs (Fig. 6d), the peak centered around 711 eV was assigned to $2p_{3/2}$ level, while the peak centered around 725 eV was set to $2p_{1/2}$ level. The Fe 2p 3/2 peak was decomposed in two components at 710.5 eV and at 712 eV which were attributed to Fe^{2+} (46 %) and Fe^{3+} (54 %), respectively [59,60]. These findings are in accordance with the results of the XRD analyses (Fig. 3) that indicated the formation of Fe_3O_4 (magnetite nanoparticles). The high-resolution C1s XPS spectrum of C-nCS@FeNPs (Fig. 6e) revealed the presence of fours components centered at 284.7, 285.9, 287.4, and 288.6 eV, which correspond to C–C/C–H (62.5 %), C–N/C–O (23.5 %), C═O (7.0 %), and O–C–O/O–C=O (7.0 %), respectively (Neves et al., 2020; Queiroz et al., 2022).

The high-resolution XPS C1s spectrum of G-FeNPs (Fig. 6f) revealed the presence of peaks centered at 284.7, 286.1, 287.9, and 288.9 eV, which correspond to C–C/C–H (57.0 %), C–N/C–O (24.6 %), C═O (10.1 %), O–C–O/O–C=O (8.3 %), respectively (Neves et al., 2020; Queiroz et al., 2022). In the high-resolution XPS Fe 2p spectrum of G-FeNPs (Fig. 6g), the two spectral peaks centered at 710.2 and 711.6 eV are attributed to $2p_{3/2}$, associated with the transition peaks centered at 723.9 and 725.9 eV in $2p_{1/2}$ region, attributed to Fe^{2+} (44 %) and Fe^{3+} (56 %), respectively [59,60]. This result is in accordance with XRD analysis, which suggested the formation of Fe_3O_4 nanoparticles. The high-resolution XPS C1s spectrum of G-nCS@FeNPs (Fig. 6h) revealed the presence of four components centered at 284.8, 285.8, 288.3, and 289.2 eV, which correspond to C–C/C–H (49.8 %), C–N/C–O (11.2 %), C═O (35.6 %), and O–C–O/O–C=O (3.4 %), respectively (Neves et al., 2020; Queiroz et al., 2022).

3.2. Magnetization curves

The magnetization curves of the pure C-FeNPs and G-FeNPs, as well

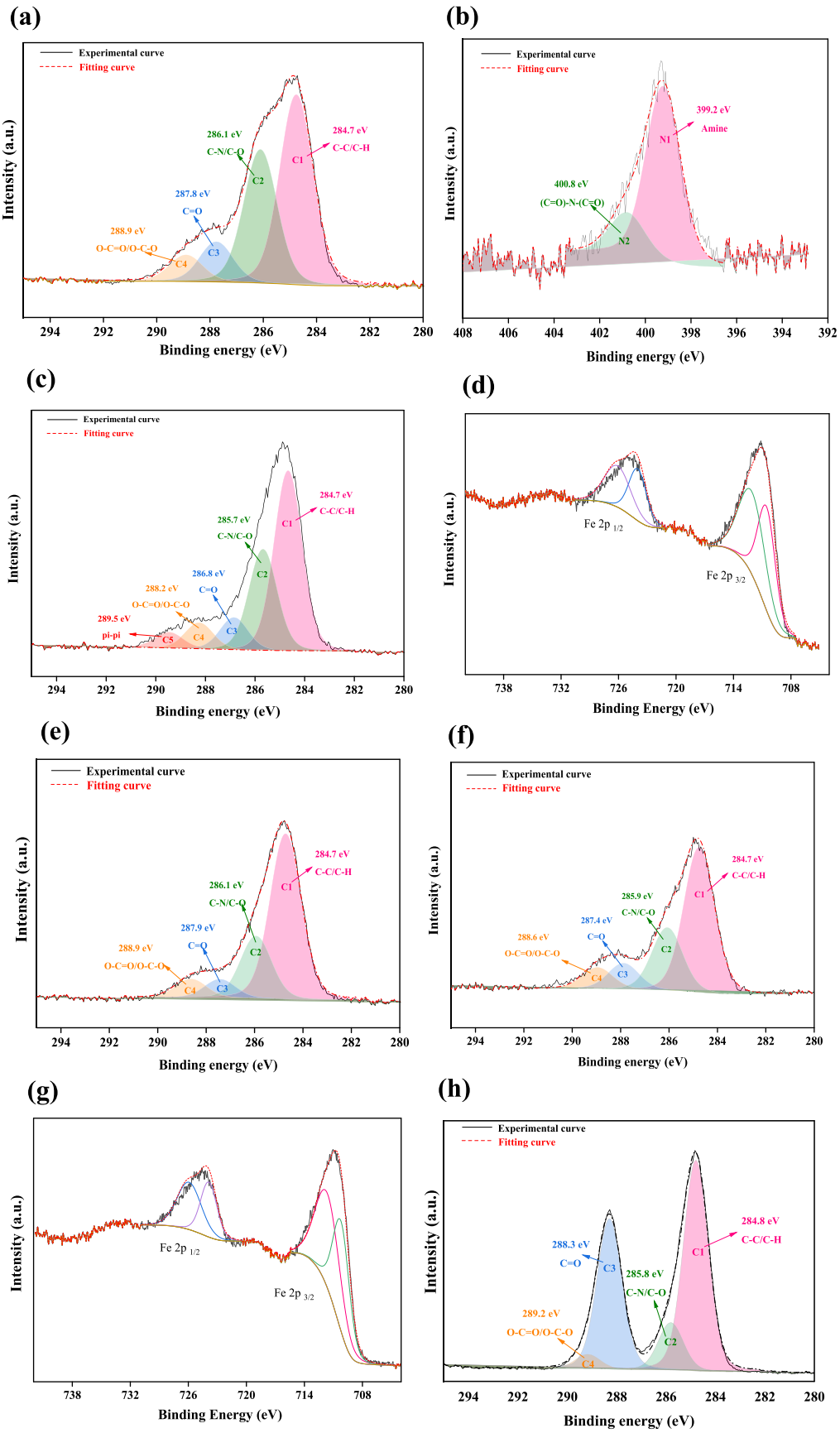

Fig. 6. XPS spectra of (a) C 1s of nCS, (b) N 1s of nCS, (c) C 1s of C-FeNPs, (d) Fe 2p of C-FeNPs, (e) C 1s of C-nCS@FeNPs, (f) C 1s of G-FeNPs, (g) Fe 2p of G-FeNPs, (h) C 1s of C-nCS@FeNPs.

Table 1
The atomic composition of nCS, C-FeNPs, G-FeNPs, C-nCS@FeNPs and G-nCS@FeNPs.

Element	Atomic composition (%)				
	Materials				
	nCS	C-FeNPs	G-FeNPs	C-nCS@FeNPs	G-nCS@FeNPs
C	43.5	63.9	37.4	36.4	57.2
O	37.0	32.2	45.0	41.8	31.5
N	1.9	–	–	0.3	0.1
Na	6.3	0.5	1.3	7.4	9.9
P	11.3	–	–	14.0	0.40
Fe	–	3.4	16.3	0.1	1.0

as their corresponding composites C-nCS@FeNPs and G-nCS@FeNPs, were measured using a vibrating sample magnetometer (VSM) as a function of the magnetic field at room temperature. The resulting data are presented in Fig. 7a-b. As evidenced by the VSM data, all materials exhibited magnetic properties. The saturation magnetization (SM) values for C-FeNPs were approximately 42 emu.g^{-1}, while those for G-FeNPs were 31 emu.g^{-1} (Fig. 7a). The decrease in MS values is related to the size of the nanoparticles [26], indicating that the FeNPs synthesized by the green method (G-FeNPs) are larger, which was confirmed by SEM images (Fig. 4). Both composites showed lower saturation magnetization values (Fig. 7b), approximately 0.008 and 0.75 emu.g^{-1} C-nCS@FeNPs, and G-nCS@FeNPs, respectively, suggesting the coating of the materials with nCS particles, corroborating the SEM analysis. Almeida et al. (2022) found a low SM value of 0.06 emu.g^{-1} in their synthesis of a magnetic composite using graphene oxide, chitosan, and organoclay [14]. Appu et al. also observed minimal saturation magnetization values for Fe_3O_4 nanoparticles (0.265 emu.g^{-1}) and a composite formed with CS (0.253 emu.g^{-1}) [27].

3.3. Assessment of adsorptive potential

C-nCS@FeNPS and G-nCS@FeNPS exhibited chemical characteristics that make them possible candidates for the removal of anionic dyes. Thus, the potentials of the adsorbents in removing the anionic dyes RR250, and RO122 were evaluated (Fig. 8).

The results indicated that the green G-nCS@FeNPs composite showed higher adsorption capacity of 178.10 mg.g^{-1} and 231.74 mg.g^{-1} for RR250 and RO122, respectively, compared to the adsorption capacity of the conventionally prepared G-nCS@FeNPs composite. The uptake capacity of C-nCS@FeNPs for RR250 and RO122 dyes was 175.17 mg.g^{-1} and 175.56 mg.g^{-1}, respectively. The superior performance of the green composite is likely attributable to its porous tridimensional structure (Fig. 4j-l) which offers a substantial surface area for interaction with the anionic dyes. In contrast, the conventionally prepared composite, C-nCS@FeNPs, formed a non-porous film, which made it more challenging for the dye molecules to access the surface. In addition, the G-nCS@FeNPs composite has a more positive surface charge, confirming the XRD analysis that the green composite has a high CS content, i.e., a high NH_2^+ content. This characteristic enables the formation of electrostatic interactions with anionic dyes, explaining the best performance of the green composite.

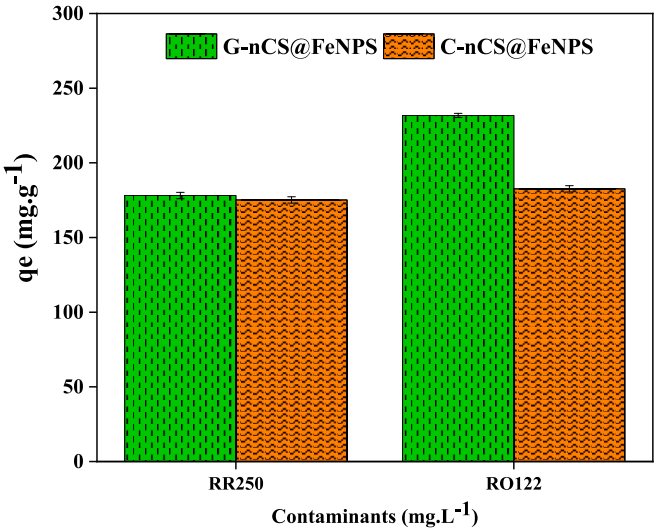

Fig. 8. Evaluation of the adsorption potential of C-nCS@FeNPs and G-nCS@FeNPs towards anionic dyes. 5 mL, RO122 and RR250 concentration of 100 mg.L^{-1}, Adsorbent concentration of 0.2 mg.mL^{-1}, 298 K, 60 min and 180 rpm. The results are mean values from triplicate assays.

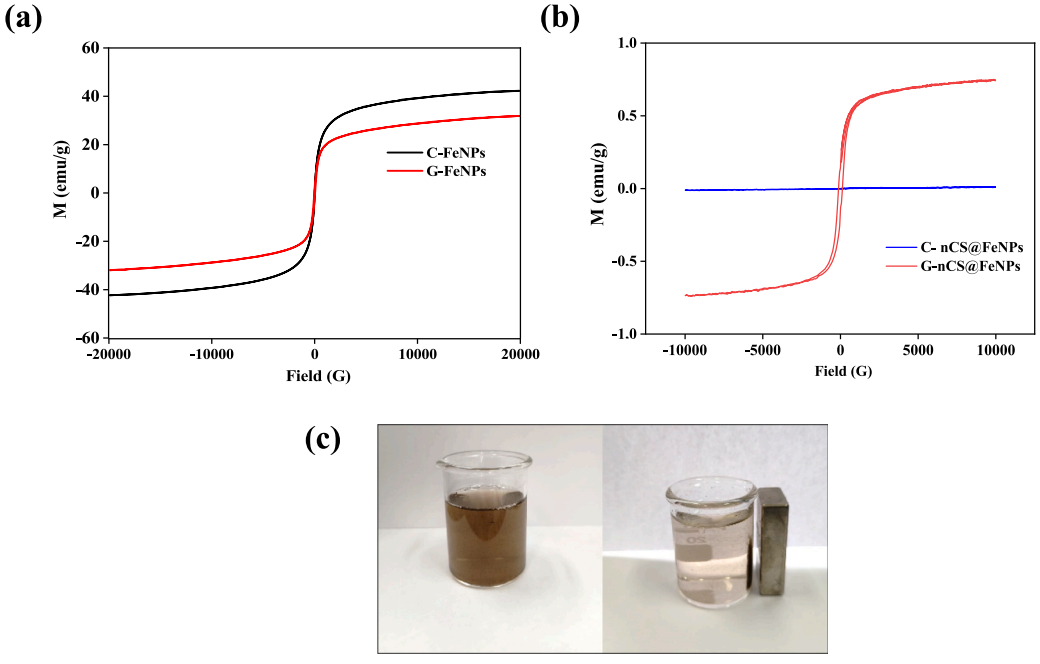

Fig. 7. Magnetization curves of (a) C-FeNPs and G-FeNPs; (b) C-nCS@FeNPs and G-nCS@FeNPs; (c) Magnetic recovery.

The results suggest that the adsorption process occurs through electrostatic and π-π interactions. The idea of electrostatic interactions is supported by the positive zeta potential values of the G-nCS@FeNPs composite (Fig. 4a), which facilitate the approximation and interactions between the anionic dyes and the G-nCS@FeNPs composite. Furthermore, the presence of aromatic rings in both dyes and proanthocyanidins indicates the potential for π-π interactions. It is established that proanthocyanidins are susceptible to interaction with contaminants via π-π interactions [15,61]. Thus, in order to gain more in-depth knowledge of the interactions between the two cationic dyes and the composite, and to find out why the RO122 dye was the most adsorbed, a study based on DFT and tests in a saline media was carried out.

3.4. Calculation of the chemical descriptors using DFT

A DFT study was conducted with the objective of achieving a comprehensive understanding of the reactivity of the two dyes employed in this work, RO122 and RR250, towards the active sites of the composite. This approach allowed for the identification of the molecular and electronic properties of the adsorbates, providing insights into the occurrence of π-π interactions between the dyes and the adsorbent [62]. The optimization of the geometry of the isolated molecules was conducted using the B3LYP/6-31G(d,p) functional hybrid in the gas phase and the optimized molecules are presented in Fig. 9. The size attributed to RO122 molecule was 30.246 Å, while for RR250 the size was 21.042 Å, indicating that RR250 is the smallest molecule. The RR250 dye demonstrated planar tendencies as a result of the conjugation of the aromatic rings. This characteristic enables high level of π-π interactions with the aromatic system of the adsorbent. In the RO122 structure, although most of the molecule is flat, the naphthalene unit bonded to two sulfonate groups is in a twisted manner with respect to the π-π system, due to the steric repulsion. The size and the conformation of the molecules directly influence their interaction with the adsorbent surface. The larger and more twisted the molecule, the more difficult it is to reach the active sites of the adsorbent, mainly through π-π interaction, which may result in a reduction in adsorption efficiency [63]. Fig. 10 shows a tridimensional rendering of the frontiers orbitals (HOMO and LUMO) for RO122 and RR250 molecules. The HOMO orbital is the occupied orbital with the highest energy, while the LUMO is the empty orbital with the lowest energy. These boundary orbitals are involved in electron transfer during adsorption. The higher the HOMO energy and the lower the LUMO energy (low band gap), the more reactive the molecule will be towards the adsorbent in terms of π-π interactions [64]. Regarding RO122, the HOMO is localized on the azo group and on the naphthyl rings attached to sulfonate groups, while LUMO is centered on the triazine ring and on the aniline attached to the sulfonate moiety. For RR250 molecule, the HOMO is concentrated on the two sulfonate groups attached to the naphthyl units, and the LUMO density occurs over the atrazine ring and on the aniline. A comparison of the band gaps of RO122 (1.1135 eV) and RR250 (1.7487 eV), respectively, shows that RO122 has the lower energy gap and it is the most reactive molecule towards the adsorbent surface.

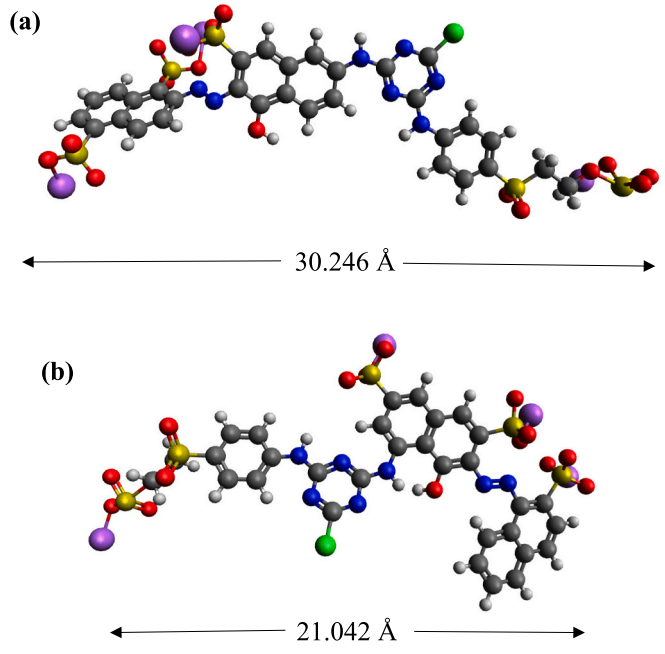

Fig. 9. Optimized structures of (a) RO122; (b) RR250.

Table 2 depicts quantum chemical parameters obtained from HOMO and LUMO energies. The chemical potential (μ) refers to the tendency of the electrons to escape from the molecule. Global chemical hardness (η) evaluates the resistance to changes in the electron distribution in a set of nuclei and electrons. And the electrophilicity index (ω) measures the molecular system's ability to receive electrons. A comparison of the data obtained for RO122 and RR250 reveals that RR250 has the highest chemical potential value (4.374 eV) and electrophilicity index (10.9450 eV). This indicates a higher tendency of RR250 to lose and accept electrons when interacting with the adsorbent surface. The RR250 exhibits greater chemical hardness (0.8741 eV), indicating that it is more resistant to variations in the electronic domains, which corroborates with the results obtained for energy gap.

The DFT study points out that the adsorption potential of the G-nCS@FeNPs composite through π-π interactions should be higher for RR250, the molecule exhibiting the most pronounced reactivity, compared to RO122. However, the experimental data indicated that RO122 was the most effectively removed contaminant (0.2240 mmol. g^{-1}), whereas RR250 exhibited a lower removal rate (0.1693 mmol. g^{-1}). The discrepancies between the calculated values and the results obtained in the adsorption experiments indicate that, in addition to π-π, other interaction mechanisms may be more significant in the removal process. Therefore, it was planned to study the adsorption in saline media to evaluate the presence of electrostatic interactions.

3.5. Adsorption experiments in saline media

As evidenced by zeta potential measurements (Fig. 5), the adsorbent G-nCS@FeNPs composite exhibits a positive surface charge. Given the anionic nature of the two dyes, it can be postulated that the predominant interactions are electrostatic in nature. To further investigate this hypothesis, adsorption tests were conducted in a saline media. In saline media, the adsorption of RO122 and RR250 was observed to occur with a qe of 0.0475 mmol.g^{-1} (78.8 % reduction) and 0.1068 mmol.g^{-1} (36.5 % reduction), respectively. These findings suggest that, in the RO122 adsorption, electrostatic interactions exert a more pronounced influence than in the RR250 adsorption, which is predominantly adsorbed by π-π interactions. Following RO122 removal, 78.8 % of interactions were found to be attributed to electrostatic interactions, whereas 22.2 % were related to π-π, hydrogen-bonding, and ion exchange. In the case of RR250 uptake, electrostatic interactions account for 36.5 % of the total interactions, while π-π interactions, hydrogen bonding, and ion exchange account for the remaining 63.5 %. According to DFT study, RR250 has a flat tridimensional arrangement, which strengthens and enables π-π interactions.

The presence of Na^+ ions in the media is likely to result in electrostatic interactions with the anionic dyes, thereby reducing their capacity to attach to the adsorbent surface. Furthermore, the negatively charged Cl^- ions may attach to the cationic sites of G-nCS@FeNPs, thereby impeding the access of the anionic dyes to the adsorbent surface [65]. It has been demonstrated that the presence of NaCl impairs electrostatic interactions [64,66]. Wu et al. [67] posit that the presence of NaCl impairs the electrostatic interactions between the neutral red (NR) dye, which is positively charged, and the D001 resin (styrene-DVB), an

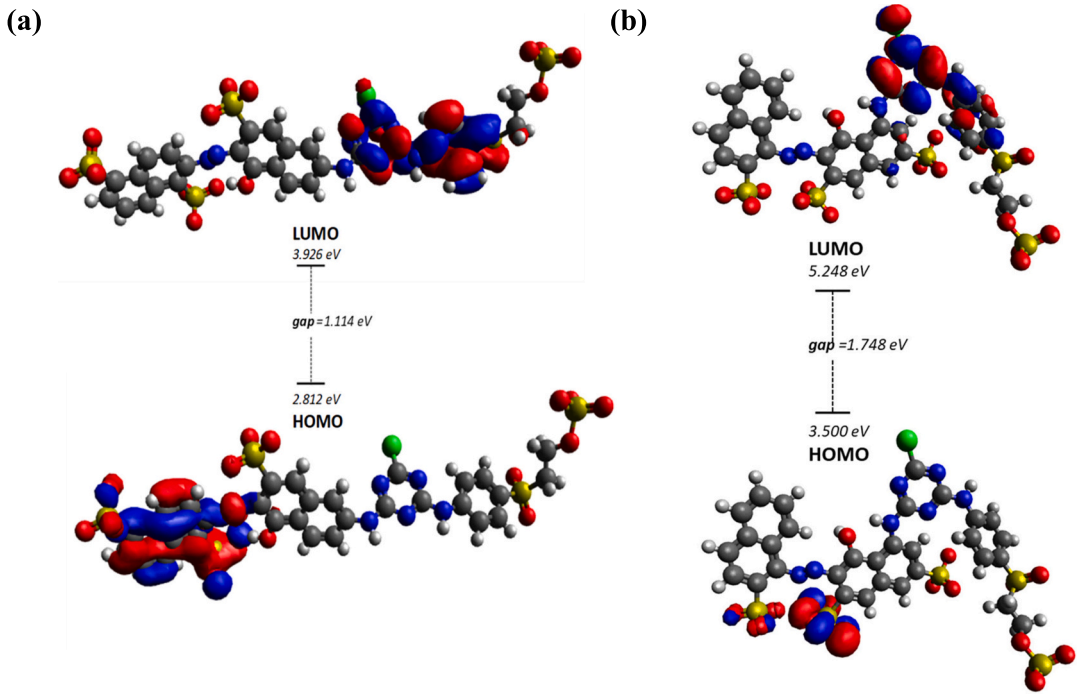

Fig. 10. Tridimensional model for the orbitals HOMO and LUMO (a) RO122; (b) RR250 (blue color: positive phase; red color: negative phase).

Table 2
– Quantum chemical parameters obtained for RO122 and RR250 dyes.

Molecular chemical descriptors	RO122	RR250
Experimental qe in water (mmol.g^{-1})	0.2240 mmol. g^{-1}	0.1693 mmol. g^{-1}
Experimental qe in saline media (mmol. g^{-1})	0.0475 mmol. g^{-1}	0.1068 mmol. g^{-1}
HOMO energy (E_H, eV)	−2.8127	−3.5002
LUMO energy (E_L, eV)	−3.9262	−5.2489
Energy gap (Δ_{H-L}, eV)	1.1135	1.7487
Chemical Potential (μ, eV)	3.3693	4.3740
Chemical hardness (η, eV)	−0.5570	−0.8741
Electrophilicity index (ω, eV)	10.1887	10.9450

anionic adsorbent. This reduction in the removal capacity of the adsorbent is attributed to the aforementioned impairment of the electrostatic interactions [67]. Avena et al. (2008) [68] reported that NaCl presence led to a competition between Na^+ and tetracycline, reducing the electrostatic interactions and consequently diminishing the adsorption rate when studying the tetracycline removal by montmorillonite. Shojaei et al. (2019) attested that the methyl orange, an anionic dye, uptake by nanodiamonds was reduced in the presence of NaCl [69]. In light of the enhanced adsorption of the RO122 dye, an investigation was conducted to ascertain the optimal adsorption parameters for this contaminant.

3.6. Assessment of operational conditions

3.6.1. pH effect

The pH variation of the solution is directly correlated with the contaminant's speciation and the adsorbent's surface charge, which are pivotal factors in the adsorption process [64,70]. Fig. 11a illustrates the charge of RO122 dye microspecies versus pH, indicating the presence of negatively charged molecules across the analyzed pH range. Fig. 11b depicts the impact of pH variation on the adsorption capacity of RO122 dye by G-nCS@FeNPs, spanning a 2 to 12 pH range.

The results obtained indicated low adsorption capacities at pH 2 and 4 of 149.8 and 154.5 mg.g^{-1}, respectively. At pH $<$ 4 the H^+ ions concentration is higher and these ions compete with the cationic adsorbent to interact with the anionic dye RO122 through electrostatic interactions [70]. At pH 6, the adsorption potential increased to 231.7 mg.g^{-1}. This phenomenon was likely caused by electrostatic interactions between the adsorbent and adsorbate, given that the composite exhibited a maximum electropositive surface charge of +36 mV (Fig. 5). Under these conditions, the number of H^+ ions in the medium is reduced, thereby limiting the competition between these ions and the adsorbent for interaction with the RO122 dye molecules. At pH 8, 10, and 12, the adsorption capacity decreased to 126.4, 105.3, and 37.4 mg.g^{-1}, respectively. Under basic conditions (pH $>$ 8), the OH^- groups present in the solution and the anionic dye molecule can compete, consequently reducing the adsorption potential [71].

Huo et al. (2021) also observed comparable outcomes with regard to the removal of the anionic methyl orange dye by a cellulose/chitosan composite film [73]. The authors reported that the acidic medium impairs the interaction of the dye with the film due to the protonation of the –NH_2 groups present in the CS and the dissociation of the sulfonated groups present in the dye molecule. In the basic medium, the authors observed that competition can occur between the anionic dye molecules and the excess hydroxide ions present in the solution. In light of these findings, the authors concluded that the highest adsorption capacity was observed at pH 6 [73]. Accordingly, the results indicate that the adsorption of RO122 dye by G-nCS@FeNPs is pH-dependent, and pH of 6 was selected as the optimal condition.

3.6.2. Sonication time effect

The impact of subjecting the G-nCS@FeNPs composite to ultrasonic waves was investigated over a period of 90 min (Fig. 12a). Prior to the adsorption tests, the material suspension was subjected to sonication. The results demonstrated that the duration of ultrasonic irradiation had a direct impact on the adsorption capacity of RO122 dye by G-nCS@FeNPs.

The absence of sonication resulted in a negative effect on RO122 removal, with an adsorption capacity of 102.9 mg.g^{-1} achieved. A number of studies have indicated that the use of ultrasonic irradiation can enhance suspension stability and dispersion [66,74]. The system was subjected to sonication for 2 min, resulting in the highest adsorption

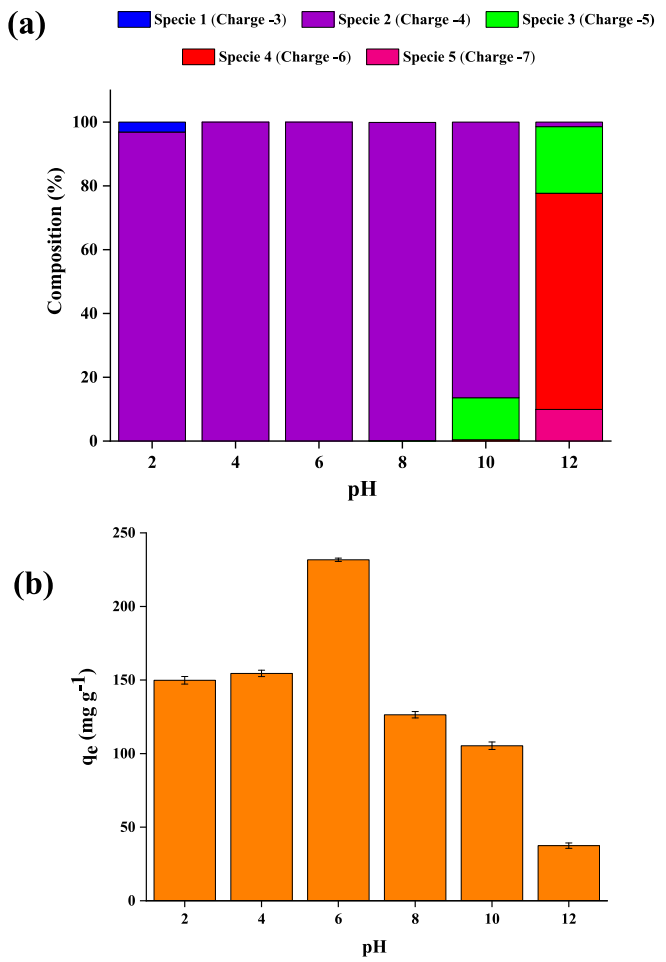

Fig. 11. **(a)** RO122 dye microspecies as a function of pH: data acquired from Chemicalize [72]; **(b)** Removal pH variation of RO122 by G-nCS@FeNPs. 5 mL, RO122 concentration of 100 mg.L^{-1}, G-nCS@FeNPs concentration of 0.2 g.L^{-1}, 2 min of sonication time, 298 K, 60 min and 180 rpm. The results are mean values from triplicate assays.

capacity (231.7 mg.g^{-1}). The stability of the suspension can result in an increase in the surface area of the material and an enhancement of active interaction sites, thereby enhancing the adsorption potential [74]. However, when the system was sonicated for 5, 10, and 15 min, the adsorption capacity decreased to 182.6, 149.8, and 107.7 mg.g^{-1}, respectively. Furthermore, a reduction in adsorption capacity was observed at times exceeding 30, 60, and 90 min, with the adsorption capacity decreasing to 79.6, 77.2, and 49.2 mg.g^{-1}, respectively. This suggests that prolonged irradiation may result in diminished removal performance, probably due to the disruption of the material's three-dimensional structure. [26]. Neves et al. (2020) [26] also observed similar results when removing basic brown 4 dye using a magnetic chitosan/quaternary ammonium salt graphene oxide composite. Also, identical behavior was observed by Silva et al. (2020) [25] in the removal of basic blue 7 dye by nanocellulose/graphene oxide nanocomposite. Accordingly, the results demonstrate that the adsorption of RO122 dye by G-nCS@FeNPs is dependent on sonication. Therefore, 2 min was selected for further investigation of the removal process.

3.6.3. Adsorbent dosage effect

The objective of this part of the study was to examine the impact in the removal system of varying the dosage of the adsorbent, which ranged from 0.1 to 0.6 g.L^{-1}. (Fig. 12b). The results showed that the RO122 adsorption was directly influenced by the variation in the adsorbent dose. The lowest adsorbent dosage of 0.1 g.L^{-1} provided the highest removal potential of 514.9 mg.g^{-1}. The concentration of G-nCS@FeNPs was increased to 0.2, 0.4, and 0.6 g.L^{-1}, resulting in a gradual decline in the removal capacity, which decreased to 210.7, 79.6, and 56.2 mg.g^{-1}, respectively. These results were expected, as increasing the adsorbent dosage decreases the unsaturation of the active sites present on the adsorbent surface [75]. Gajera et al. (2022) observed a comparable profile in the removal of Congo red anionic dye by a TiO_2-loaded fly ash chitosan composite. Accordingly, the optimal amount of adsorbent for the adsorption system was determined to be 0.1 g.L^{-1} [76].

3.6.4. Effect of the contact time

The impact of contact time on the adsorption of RO122 by G-nCS@FeNPs was investigated over 150 min (Fig. 12c). The adsorption process was observed to proceed through three distinct phases. Initially, rapid adsorption occurred during the first minutes. This was followed by a period of constant adsorption rate, and finally, a decrease in adsorption performance. The highest removal potential for RO122 dye was reached at 10 min when the adsorption capacity was 608.6 mg.g^{-1}. The removal potential remained constant up to 45 min (between ~608.6 to 603.9 mg.g^{-1}).

Subsequently, a reduction in RO122 uptake was noted, and equilibrium was reached within 60 min (514.9 mg.g^{-1}), attributable to the desorption of contaminant molecules. [77]. In a study conducted by Ilhan et al. (2008), the optimal time for the removal of RO122 by dried cells of *Penicillium restricum* was found to be 75 min [78]. Saeed et al. (2015) synthesized a biosorbent based on chemically treated *Trapa bispinosa* and applied it to the removal of RO122 [2]. The authors reported an equilibrium time of 120 min, 12 times longer than that observed in this study. Although equilibrium was reached within 60 min, the optimal time for the adsorption of RO122 by G-nCS@FeNPs was 10 min, during which the highest removal capacity was achieved. These findings are encouraging, as rapid contaminant removal is among the desirable parameters for the adsorption process.

3.6.5. Temperature effect

Experiments were conducted to assess the effect of temperature on the adsorption of RO122 by G-nCS@FeNPs composite within the temperature range of 298 to 328 K (Fig. 12d). The obtained results indicated that the temperature directly influenced the adsorption of RO122 dye by G-nCS@FeNPs.

The highest adsorption potential was reached at 298 K (608.6 mg.g^{-1}). Increasing the temperature to 308, 318 and 328 K impaired the removal process, decreasing the adsorption capacity to 571.2, 561.8, and 524.3 mg.g^{-1}, respectively. High temperatures are known increase the molecular agitation of the system [79], which increases the kinetic energy of the molecules, hinders the adsorbent/adsorbate interactions, and consequently damages the adsorption process [14,64]. These results indicated an exothermic profile of the system since the increase in temperature was detrimental to the process [70,80]. In our previous works, the same trend was observed in the removal process of several organic dyes, such as basic blue 7 [66], basic blue 26 [70], basic brown 4 [26], and direct black 22 [64].

3.7. Kinetic modeling

The adsorption process of RO122 dye by G-nCS@FeNPs was investigated by analyzing the kinetic profile. Nonlinear models, including pseudo-first order (PFO) [81] and pseudo-second order (PSO) [82], were used to fit the experimental data. The degree of fit was determined from the correlation coefficient (R^2) and Akaike Information Criterion (AIC). The equilibrium was reached in 60 min for the removal systems at concentrations of 100, 200, and 300 mg.L^{-1}, and the experimental adsorption capacities were 608.6, 1978.3, and 2359.6 mg.g^{-1}, respectively. The results obtained are presented in Table 3.

Table 3 shows that the PSO model fits the experimental data better,

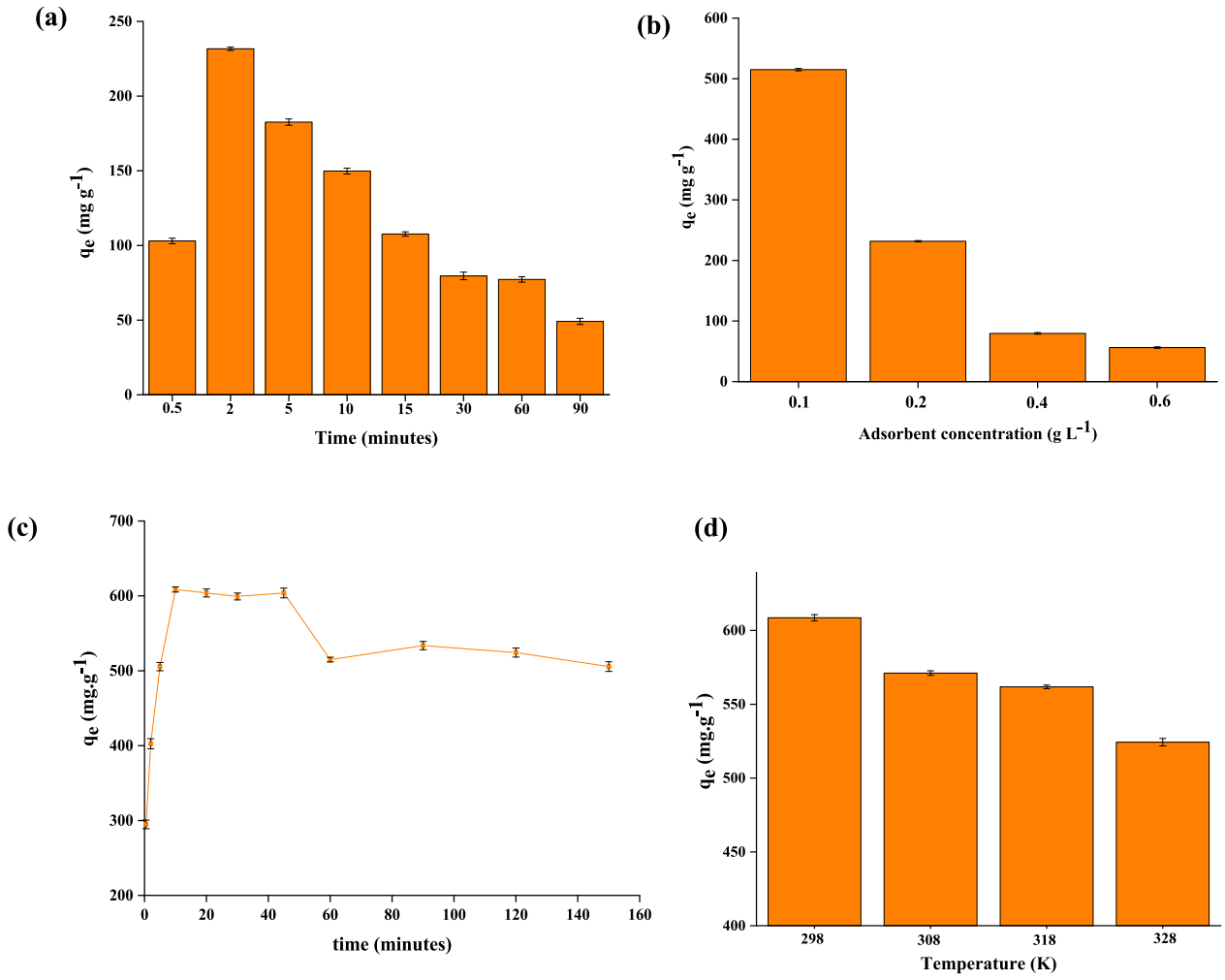

Fig. 12. All tests were conducted with a RO122 concentration of 100 mg.L^{-1}, 5 mL, pH 6, 180 rpm. The results are mean values from triplicate assays. **(a)** Sonication time variation in the removal of RO122 by G-nCS@FeNPs concentration of 0.2 g.L^{-1}, 298 K and 60 min; **(b)** Adsorbent concentration variation in the removal of RO122 by G-nCS@FeNPs. 298 K, 60 min, and 2 min of sonication time; **(c)** Contact time variation in the removal of RO122 by G-nCS@FeNPs concentration of 0.1 g. L^{-1}, 298 K, 2 min of sonication time; **(d)** Temperature variation in the removal of RO122 by G-nCS@FeNPs concentration of 0.1 g.L^{-1}, 10 min, and 2 min of sonication time.

Table 3
Kinetic parameters in the adsorption process.

RO122 concentration (mg.L^{-1})				
		100	200	300
Experimental (q_e)		608.6	1978.3	2359.6
PFO	k^{-1}	1.0222	9.7318	5.8990
	q_e	529.0300	1974.5606	2403.0957
	R^2	0.8803	0.9995	0.9936
	R^2_{adj}	0.8683	0.9995	0.9929
	AIC	−54.15	−57.41	−55.52
PSO	k^{-1}	1.3041	202.7090	35.0187
	q_e	598.4220	1977.5291	2421.0734
	R^2	0.9408	0.9996	0.9935
	R^2_{adj}	**0.9349**	**0.9995**	**0.9929**
	AIC	−51.27	−93.08	−53.02

with R^2_{adj} ranging from 0.9349 to 0.9995 and AIC ranging from −51.27 to −93.08. This model predicted equilibrium adsorption capacities of 598.42, 1977.52, and 2421.07 mg.g^{-1} for the 100, 200, and 300 mg.L^{-1} concentrations, respectively, adsorption capacities similar to the experimental values. The best fits were observed for the highest concentrations, 200 and 300 mg.L^{-1}. The PSO model suggests that the adsorption rate is contingent upon the interactions between the adsorbent active sites and the adsorbent [83], and that the adsorbent and the adsorbate have strong interactions at multiple active sites [26,84].

In their study of the uptake of methyl orange anionic dye by magnetic chitosan nanoparticles, Hosseini et al. observed that the PSO model demonstrated the best correlation with the experimental kinetic data [85]. In this study the maximum removal capacity was 20.5 mg.g^{-1}. Similarly, Selim et al. (2022) [86] achieved comparable results in their investigation into the preparation of a composite comprising nanochitosan and its application in the removal of Congo red anionic dye from wastewater. The kinetic model that provided the best fit to the experimental data was the PSO, and the maximum removal capacity was determined to be 230 mg.g^{-1}.

3.8. Isothermal modeling

The isothermal study was carried out at temperatures 298, 308, and 318 K, under the optimal conditions determined previously, and the results obtained are presented in Fig. 13. The adsorption isotherms for all temperatures were classified as L3, following the Giles classification [87]. Initially, there is rapid initial adsorption of the dye by G-nCS@FeNPs, as evidenced by the initial slope of the curves. After saturation (inflection point), the isotherms show increased adsorption

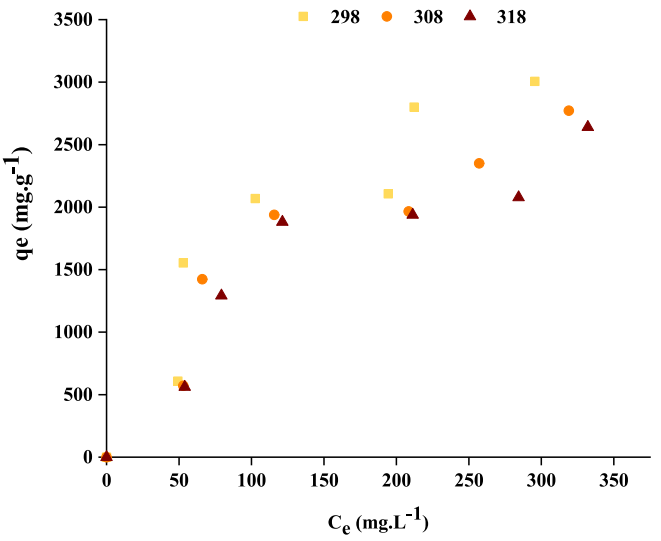

Fig. 13. Adsorption isotherms were measured at temperatures of 298 K, 308 K, and 318 K. G-nCS@FeNPs concentration of 0.1 g.L^{-1}, 10 min, and 2 min of sonication time.

capacity with increasing dye concentration. This suggests that adsorption may initially occur in monolayers and after the inflection point, the initially adsorbed dye molecules may promote new interactions that favor adsorption in multilayers [87,88].

The Langmuir, Freundlich, Redlich-Peterson, D-R, and Temkin models were fitted to experimental data to understand the adsorption behavior, and the results obtained are presented in Table 4. The applicability of the models was assessed based on the correlation coefficients obtained (R^2).

The D-R model suggests physical adsorption in the process [89]. At 298 K and 308 K, the D-R model best fitted the experimental data, indicating the formation of multilayers through physisorption. These findings are in accordance with those of previous studies, which suggest that electrostatic and π–π interactions are significant factors influencing RO122 uptake. At 318 K, the experimental adsorption data was fitted by the Temkin model, suggesting the formation of a homogeneous saturated layer on the adsorbent surface at high temperatures.

The greatest adsorption capacity was achieved at 298 K (3005.62 mg.g^{-1}), followed by 308 K (2771.53 mg.g^{-1}) and 318 K (2640.45 mg.g^{-1}). These results indicate that increasing temperature negatively affected the performance of G-nCS@FeNPs in removing RO122 dye, suggesting an exothermic effect. At low temperatures, physisorption is generally favored [90]. The nCS provided protonated amines that interact with the anionic portion of the RO122 dye, enabling greater proximity between the adsorbent/adsorbate, which can favor other types of interactions, such as π–π interactions and hydrogen bonds [91].

The greatest removal efficiency of RO122 by G-nCS@FeNPs was selected for comparison with the performance of other adsorbents. Different adsorbents were selected for comparison, and their respective capacities are shown in Table 5. Compared with values reported in the literature, the composite of nCS and FeNPs synthesized by the green method (G-nCS@FeNPs) showed a higher adsorption capacity for the RO122 dye. Which is approximately 10 times greater than the highest reported adsorption capacity, indicating that the material easily produced in this study is promising for dye removal. The composite, G-nCS@FeNPs, exhibited a markedly high adsorption capacity in just 10 min of contact, a notable contrast to other adsorbents, such as Beads of *Trapa bispinosa's peel*-H_2O_2 and Beads of *Trapa bispinosa's* fruit-H_2O_2, which require considerably longer periods, approximately 120 min, to reach an adsorption capacity of approximately 90 mg.g^{-1}. This efficiency suggests that G-nCS@FeNPs could serve as a promising alternative for water treatment and pollutant removal.

3.9. Thermodynamic study

The thermodynamic parameters of Gibbs energy (ΔG°), enthalpy (ΔH°), and entropy (ΔS°) changes were determined by analyzing the adsorption process of RO122 dye by G-nCS@FeNPs at temperatures of 298 K, 308 K, and 318 K. The calculation of thermodynamic parameters, ΔH° and ΔS°, is based on the slope and intercept, respectively, of the linear regression of ln(K) versus (1/T) (Fig. 14). The results are summarized in Table 6.

The thermodynamic parameters obtained suggest spontaneity in the adsorption system, indicated by the negative values of ΔG° [54,64]. In general, the variation in Gibbs free energy for physisorption is between −20 and 0 kJ mol^{-1}, whereas for chemisorption, it is within the range of −80 to −400 kJ mol^{-1} [94]. Accordingly, the values for ΔG° in this study were approximately −5 kJ.mol^{-1}, which suggests that physisorption is the main operating mechanism. These findings are in accordance with the previously obtained results, which indicate that the RO122 adsorption process is primarily mediated by electrostatic and π-π interactions. Moreover, a slight increase in ΔG° values is observed from 298 K to 318 K, suggesting that the increase in temperature not favor the adsorption process [95]. This finding aligns with the observations documented in the temperature effect section (Fig. 12d).

The negative value of ΔH° indicates that the adsorption of RO122 dye by G-nCS@FeNPs is exothermic, i.e., high temperatures may

Table 4
Isothermal parameters in the adsorption process.

Models	Parameters	Temperature (K)		
		298	308	318
Langmuir	q_m (mg.g^{-1})	3547.66	3248.60	2586.66
	K_L (L.mg^{-1})	0.0133	0.0111	0.0154
	R^2	0.8020	0.8367	0.8394
Freundlich	n_F	0.3727	0.3803	0.3898
	K_F [(mg.g^{-1}).(Lmg^{-1})) $1/n_F$]	351.1761	291.3478	253.9470
	R^2	0.8432	0.8815	0.8229
Redlich-Peterson	K_{RP} (L/g)	47.7073	44.6917	40.7718
	α (L/mg)$^{\beta}$	135.6711	153.2701	160.3747
	β (dimensionless)	0.6275	0.6198	0.6103
	R^2	0.8432	0.8814	0.8228
D-R	q_{D-R} (mg.g^{-1})	3138.81	2502.06	2486.07
	K_{D-R}	0.0007	0.0005	0.0007
	R^2	**0.9944**	**0.9410**	0.9395
Temkin	K_T	0.1299	0.1055	0.0827
	RT/b	783.9230	728.1290	727.3103
	R^2	0.9796	0.8603	**0.9805**

Table 5
Comparison data on the removal of the anionic dye RO122 by different adsorbents.

Material	Conditions	q_e (mg.g^{-1})	Reference
Hectorite-cetyldimethyl benzylammonium chloride	60 mg.L^{-1} (dye)	55.49	[92]
Hectorite-cetylpyridinium chloride	100 mg.L^{-1} (dye)	67.15	
Beads of *Trapa bispinosa*'s peel-H_2O_2	120 min	72.60	[2]
Beads of *Trapa bispinosa*'s fruit-H_2O_2	120 min	84.4	
Polyviologen polymer	20 mg.L^{-1} (dye), 30 min	56	[93]
CS@CNC–mTA bead	100 mg.L^{-1} (dye), 150 min	311	[70]
G-nCS@FeNPs	600 mg.L^{-1} (dye), 10 min	3005.62	**This work**

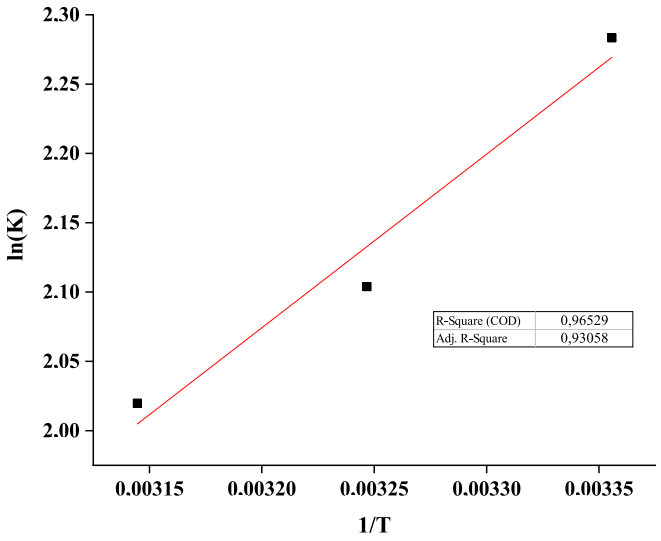

Fig. 14. Fitting of the thermodynamic parameters of the adsorption of RO122 by G-nCS@FeNPs.

Table 6
Thermodynamic parameters of RO122 on G-nCS@FeNPs at 298, 308 and 318 K.

ΔG° (kJ.mol^{-1})			ΔH° (kJ.mol^{-1})	ΔS° (kJ.mol^{-1})
298 K	308 K	318 K		
−5.6570	−5.2125	−5.0044	−10.4133	−0.0160

disfavor the adsorption process [70]. In consideration of the ΔH° values, those that are <80 kJ.mol^{-1} are indicative of physical adsorption processes, while those that exceed 80 kJ.mol^{-1} are ascribed to chemical adsorption processes [96]. Thus, according to the ΔH° value (−10.41 kJ.mol^{-1}), the RO122 uptake by the G-nCS@FeNPs occurs by the physisorption process [96,97]. The negative value of ΔS° reveals the regularity of RO122 molecules at the adsorbent interface at low temperatures [66].

3.10. Multicomponent system

To date, the G-nCS@FeNPs composite has demonstrated remarkable efficacy in the removal of the RO122 dye in a single adsorption system. In this study, the performance of the adsorbent in removing RO122 in real multicomponent systems was investigated. To this end, a real sample collected from the Ribeirão Pinhal River was spiked with RO122 at a 5 mg.L^{-1}. Even in complex matrices, G-nCS@FeNPs demonstrated a 51 % RO122 removal efficiency.

In order to investigate the effect of RO122 removal in the presence of a cationic (safranin, SF) and anionic (RR250) dye, experiments were carried out in binary systems under the best conditions obtained in the previous tests. The results obtained are shown in Fig. 15. The G-nCS@FeNPs composite showed removal potential for anionic dyes in single adsorption systems and the adsorption capacity for RO122 and RR250 was 608 and 366 mg.g^{-1}, respectively. However, the adsorbent did not show adsorption potential for the cationic dye SF in a single adsorption system. These results were expected since the adsorbent had an electronegative surface charge (Fig. 5), which contributes to the electrostatic repulsion between the composite and the SF.

In the binary system, a competitive effect was observed between the anionic dyes RO122 and RR250, since the adsorption performance of the dyes decreased from 608 to 329 mg.g^{-1} and 366 to 274 mg.g^{-1}, respectively. Interestingly, a synergistic effect was observed when the cationic dye SF coexisted with the anionic dye RO122. For SF dye, the

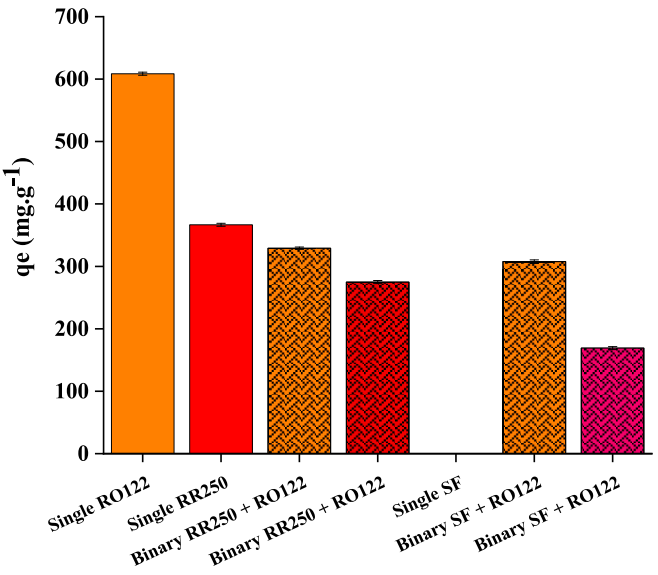

Fig. 15. Adsorption of RO122 in a multicomponent system. G-Ncs@FeNPs concentration of 0.1 g.L-1, 298 K, 2 min of sonication time, 10 min of contact time, pH 6 and 180 rpm.

adsorption performance increased from 0 to 169 mg.g^{-1}. Probably, RO122 is initially adsorbed, and the anionic dye remains adsorbed on the adsorbent surface. This may reduce the electrostatic repulsion of the cationic portion of the adsorbent with the SF, allowing the dye to approach and subsequently be removed. Nevertheless, additional research is required to gain a deeper understanding of the adsorption process between the material and emerging contaminants.

3.11. Study of the mechanism of the uptake of RO122 by G-nCS@FeNPs

The uptake mechanism of RO122 was investigated using XPS and FTIR, as shown in Fig. 16. The FTIR spectrum of G-nCS@FeNPs after RO122 adsorption revealed some modifications compared to the spectrum of the pristine adsorbent. The band at 3420 cm^{-1}, related to the OH and NH functional groups, shifted to 3363 cm^{-1}, suggesting that hydrogen bonds occurred between the NH and OH moieties of the adsorbent and RO122. Also, the intensity of this band increased after adsorption, due to the presence of the NH and OH groups of the RO122 dye. Also, it appeared at the 1128 cm^{-1} band, which is attributed to the

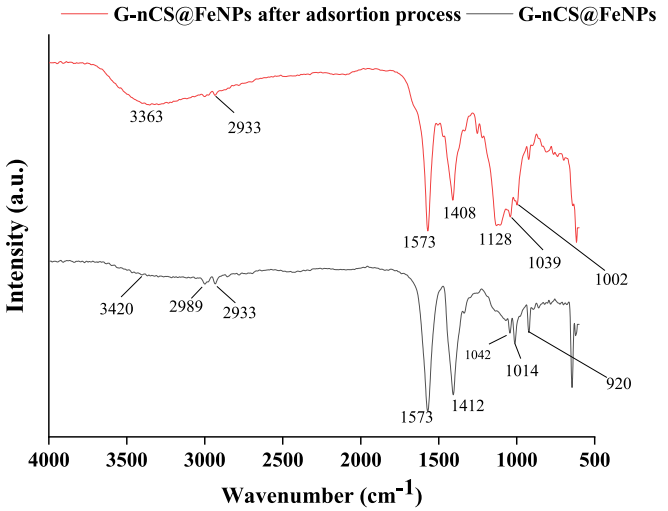

Fig. 16. FTIR spectra of G-nCS@FeNPs before and after RO122 uptake.

presence of S═O asymmetric stretching in SO_3^- groups [98] of the RO122 molecules. The bands at 1042 and 1014 cm^{-1}, referred to as C–O–C of nCS and PAS [43], blue-shifted to 1039 and 1002 cm^{-1} after RO11 uptake, suggesting that ether groups interact through H–bonds with the OH and NH groups of RO122 dye.

XPS survey analysis after RO122 adsorption showed some variations in the chemical composition (Table 7). The appearance of S and the increase in Cl and N content confirm the presence of RO122 molecules attached to G-nCS@FeNPs. The reduction in P and Na contents suggests that the anionic molecules of RO122 may have displaced the tripolyphosphate anions bound to CS, through an anion exchange mechanism.

XPS high-resolution C1s after RO122 removal (Fig. 17 and Table 8) revealed that the contents C–C/C=C and C–N/C–O increased slightly, from 49.8 to 54.0 %; and from 11.2 to 16.2 %, due to the presence of dye molecules. Regarding XPS high-resolution O 1 s, a reduction in the oxygen content bound to Na/P is noted, corroborating the ion exchange mechanism. The carboxyl peak, centered at 534.9 eV, shifted to 534.2 eV after RO122 adsorption, indicating that C=O(O) of FeNPs may act as an H–bonding acceptor for NH and OH groups of the dye.

Based on the data obtained through DFT, experiments in saline media, and FTIR and XPS analyses after the adsorption process, a proposed mechanism is presented in Fig. 18. The results indicate that the adsorption of RO122 on the surface of G-nCS@FeNPs is primarily driven by electrostatic interactions and anion exchange. The presence of SO_3^- groups in the structure of RO122 is of considerable consequence in this process, as these negatively charged groups interact with the positively charged NH_3^+ groups in the composite. This interaction indicates a robust affinity between the dye and the adsorbent, which facilitates effective adsorption. Additionally, hydrogen bonding plays a notable role in the adsorption mechanism. The interaction between the NH and OH portions of the G-nCS@FeNPs adsorbent with the functional groups of RO122 may enhance the stability of the adsorbed layer, thereby facilitating the binding process. Moreover, π-π interactions contribute to the adsorption process. The aromatic rings present in RO122 are capable of interacting with the aromatic rings present in the composite structure. Nevertheless, this combination of interactions substantiates the efficacy of the G-nCS@FeNPs composite as an adsorbent.

4. Conclusions

New composites of nanochitosan and iron nanoparticles synthesized by conventional (C-nCS@FeNPs) and green (G-nCS@FeNPs) methods were prepared, characterized, and used to remove anionic dyes. The composite synthesized by the green method showed better removal capacity for RO122 and RR250 dyes, due to its more electropositive surface, tridimensional porous structure and higher CS content.

The affinity of the two dyes for G-nCS@FeNPs was observed to be more pronounced for RO122 (231.7 $mg.g^{-1}$) than for RR250 (178.0 $mg.g^{-1}$), despite the high similarity between the two molecules. The DFT study indicated RR250 as the more susceptible dye to be adsorbed through π-π interactions. While experiments in saline media revealed that 78.8 % of the interactions between RO122 and the adsorbate are based on electrostatic, e the rest is attributed to π-π, hydrogen-bonding, and ion exchange. Regarding the removal of RR250 dye, 36.5 % of the interactions were found to be attributable to electrostatic interactions,

Table 7
Obtained data for XPS survey before and after RO122 uptake.

Element	Composition before adsorption (%)	Composition after adsorption (%)
C	57.2	56.5
O	31.5	31.2
N	<0.1	1.4
Na	10.9	8.3
P	0.25	0.1
Cl	0.15	0.8
S	–	1.7

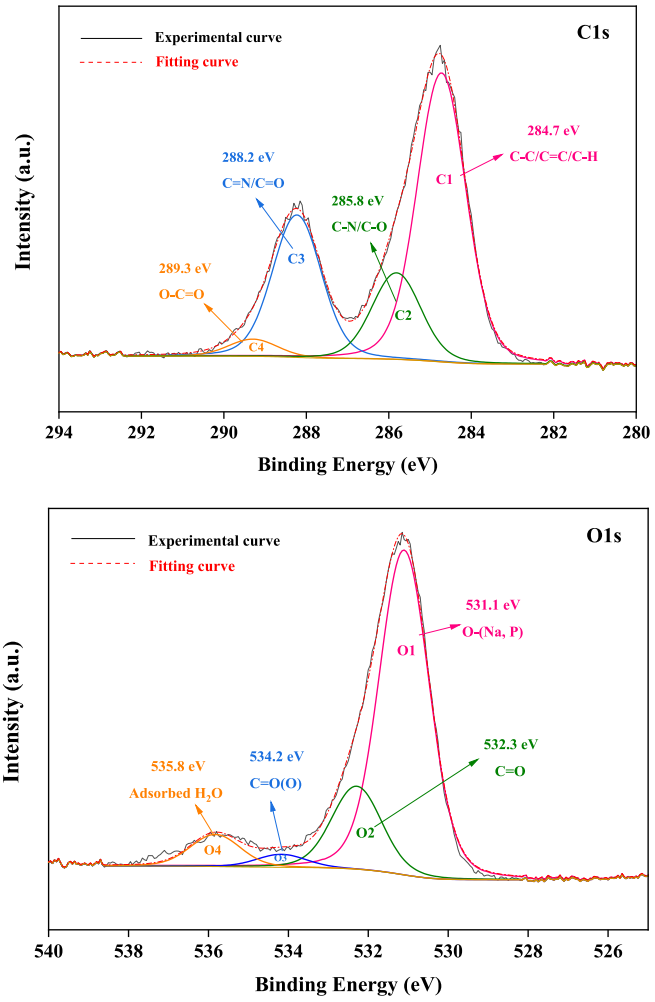

Fig. 17. XPS spectra of G-nCS@FeNPs after RO122 uptake.

Table 8
High-resolution C1s data for G-nCS@FeNPs before and after RO122 adsorption.

G-nCS@FeNPs		G-nCS@FeNPs/RO122		
Binding energy (eV)	Composition (%)	Binding energy (eV)	Composition (%)	Carbon group
284.8	49.8	284.7	54.0	C–C/C=C/C–H
285.8	11.2	285.8	16.2	C–O/C–N
288.3	35.6	288.2	26.6	C=N/C=O
289.2	3.4	289.3	3.2	O–C=O
531.1	79.1	531.1	71.7	O-(Na, P)
532.3	11.8	532.3	18.3	C=O
534.9	3.4	534.2	2.9	C=O(O)
536.0	5.7	535.8	7.1	Adsorbed H_2O

whereas 63.5 % were ascribed to the aforementioned interactions.

The parameters of the process were varied for the best system, RO122 and the G-nCS@FeNPs composite. In a remarkably brief 10 min, at pH 6 and room temperature, an exceedingly high adsorption potential was achieved (3005.62 $mg.g^{-1}$), indicating the composite as a potential adsorbent for the uptake of anionic dyes. The experimental kinetic data for the adsorption of the anionic dye RO122 was best described by the pseudo-second order model, indicating strong interactions between the adsorbent and the dye in multiple active interaction sites. According to Giles' classification, the adsorption isotherms were classified as L3. The D-R isothermal model provided the best fit to the experimental data at

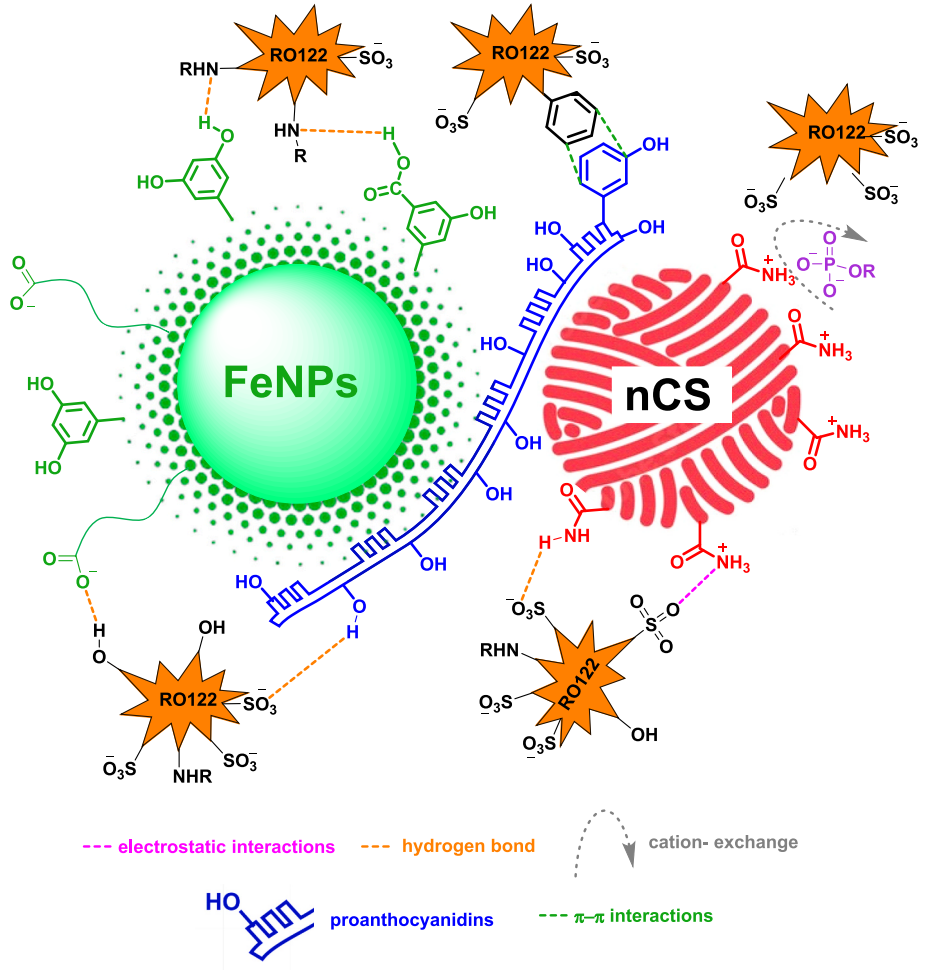

Fig. 18. Proposed mechanism for the adsorption of RO122 dye by G-nCS@FeNPs.

room temperature, while the Temkin model was the best fit to increasing temperature. The thermodynamic parameters obtained suggest that the RO122 adsorption process by G-nCS@FeNPs occurs spontaneously through physisorption.

The study of mechanism based on DFT, experiments in saline media, and XPS and FTIR analyses post adsorption, suggests that the RO122 adsorption on the nCS@FeNPs surface is primarily driven by electrostatic interactions and anion exchange, with hydrogen bonding and π–π interactions also contributing to the process.

CRediT authorship contribution statement

Natália Gabriele Camparotto: Writing – review & editing, Writing – original draft, Software, Methodology, Investigation, Funding acquisition, Formal analysis, Data curation, Conceptualization. **Gabriel Henrique Silva Fulaneti:** Writing – original draft, Investigation, Data curation. **Harold Hilarion Fokoue:** Visualization, Software, Investigation, Data curation. **Valmor Roberto Mastelaro:** Software, Formal analysis, Data curation. **Melissa Gurgel Adeodato Vieira:** Writing – review & editing, Validation, Supervision, Project administration, Methodology, Funding acquisition. **Patrícia Prediger:** Writing – review & editing, Writing – original draft, Visualization, Validation, Supervision, Project administration, Methodology, Funding acquisition, Data curation, Conceptualization.

Declaration of competing interest

The authors declare that they have no known competing financial interests or personal relationships that could have appeared to influence the work reported in this paper.

Acknowledgments

The authors would like to express their gratitude to the Coordination for the Improvement of Higher Education Personnel (CAPES, Financial code – 001), the São Paulo State Foundation (FAPESP) (numbers 2023/02041-8, 2022/14834-0, 2013/07296-2), the National Council for Scientific and Technological Development (CNPq) (numbers 308046/2016-6, 311419/2022-4, 403211/2023-9), and the Teaching, Research and Extension Support Fund (FAEPEX) (numbers 2207/23, 2529/23). For SEM analysis, Josiane Aparecida de Souza Vendemiatti was responsible, while Dr. Ausdinir Bortolozo conducted the XRD analyses. The zeta potential analysis was carried out at the National Bio-renewables Laboratory (LNBR/CNPEM). The authors thank the Espaço da Escrita - UNICAMP for their invaluable help with language services.

Appendix A. Supplementary data

Supplementary data to this article can be found online at https://doi.org/10.1016/j.ijbiomac.2024.138657.

References

[1] M.S. Anantha, S. Olivera, C. Hu, B.K. Jayanna, N. Reddy, K. Venkatesh, H. B. Muralidhara, R. Naidu, Comparison of the photocatalytic, adsorption and electro- chemical methods for the removal of cationic dyes from aqueous solutions,

Environ. Technol. Innov. 17 (2020) 100612, https://doi.org/10.1016/J.ETI.2020.100612.
[2] M. Saeed, R. Nadeem, M. Yousaf, Removal of industrial pollutant (Reactive Orange 122 dye) using environment-friendly sorbent Trapa bispinosa's peel and fruit, Int. J. Environ. Sci. Technol. 12 (2015) 1223–1234, https://doi.org/10.1007/S13762-013-0492-9/ FIGURES/7.
[3] A. Khan, A. Roy, S. Bhasin, T. Bin Emran, A. Khusro, A. Eftekhari, O. Moradi, H. Rokni, F. Karimi, Nanomaterials: an alternative source for biodegradation of toxic dyes, Food Chem. Toxicol. 164 (2022) 112996, https://doi.org/10.1016/J.FCT.2022.112996.
[4] C. Jeyaseelan, M. Kaur, M. Sen, Activated carbon modified chitosan beads: an effective method for removal of Congo Red dye, Mater. Today Proc. (2023), https://doi.org/10.1016/J.MATPR.2023.03.802.
[5] S. Mittal, A. Roy, Fungus and plant-mediated synthesis of metallic nanoparticles and their application in degradation of dyes, Photocatalytic Degrad Dye. Curr. Trends Futur. Perspect. (2021) 287–308, https://doi.org/10.1016/B978-0-12-823876-9.00009-3.
[6] J. Zhan, H. Sun, L. Chen, X. Feng, Y. Zhao, Flexible fabrication chitosan-poly-amidoamine aerogels by one-step method for efficient adsorption and separation of anionic dyes, Environ. Res. 234 (2023) 116583, https://doi.org/10.1016/J.ENVRES.2023.11 6583.
[7] D. Bertagna Silva, A. Cruz-Alcalde, C. Sans, J. Giménez, S. Esplugas, Performance and kinetic modelling of photolytic and photocatalytic ozonation for enhanced micropollutants removal in municipal wastewaters, Appl. Catal. B Environ. 249 (2019) 211–217, https://doi.org/10.1016/J.APCATB.2019.02.072.
[8] Z. Zaheer, A.S. Al-Shehri, A.M. Alsudairi, S.A. Kosa, Silver-ruthenium bimetallic nanoparticles as sacrificial heterogeneous persulfate activator in situ chemical oxidation of dye, J. Mol. Liq. 377 (2023) 121549, https://doi.org/10.1016/J.MOLLIQ.2023.121549.
[9] Y.C. Wang, S.R. Kumar, C.M. Shih, W.S. Hung, Q.F. An, H.C. Hsu, S.H. Huang, S. J. Lue, High permeance nanofiltration thin film composites with a polyelectrolyte complex top layer containing graphene oxide nanosheets, J. Membr. Sci. 540 (2017) 391–400, https://doi.org/10.1016/j.memsci.2017.06.074.
[10] A. Kausar, S.T. Zohra, S. Ijaz, M. Iqbal, J. Iqbal, I. Bibi, S. Nouren, N. El Messaoudi, A. Nazir, Cellulose-based materials and their adsorptive removal efficiency for dyes: a review, Int. J. Biol. Macromol. 224 (2023) 1337–1355, https://doi.org/10.1016/J.IJBIOMAC.2022.10.220.
[11] P. Pourhakkak, A. Taghizadeh, M. Taghizadeh, M. Ghaedi, S. Haghdoust, Fundamentals of adsorption technology, Interface, Sci. Technol. 33 (2021) 1–70, https://doi.org/10.1016/B978-0-12-818805-7.00001-1.
[12] O.P. Bolade, A.B. Williams, N.U. Benson, Environmental nanotechnology, monitoring & management green synthesis of iron-based nanomaterials for environmental remediation : a review, Environ. Nanotechnology, Monit. Manag. 13 (2020) 100279, https://doi.org/10.1016/j.enmm.2019.100279.
[13] P. Prediger, T. de Figueiredo Neves, N.G. Camparotto, E.A. Rodrigues, Green nanomaterials for environmental remediation, in: Handb. Green Sustain. Nanotechnol, Springer International Publishing, Cham, 2022, pp. 1–34, https://doi.org/10.1007/978-3-030-69023-6_23-1.
[14] A. da S.V. de Almeida, T. de Figueiredo Neves, M.G.C. da Silva, P. Prediger, M.G. A. Vieira, Synthesis of a novel magnetic composite based on graphene oxide, chitosan and organoclay and its application in the removal of bisphenol A, 17α-ethinylestradiol and triclosan, J. Environ. Chem. Eng. 10 (2022) 107071, https://doi.org/10.1016/J.JECE.2021.107071.
[15] R.N. Queiroz, T. de F. Neves, M.G.C. da Silva, V.R. Mastelaro, M.G.A. Vieira, P. Prediger, Comparative efficiency of polycyclic aromatic hydrocarbon removal by novel graphene oxide composites prepared from conventional and green synthesis, J. Clean. Prod. 361 (2022) 132244, https://doi.org/10.1016/J.JCLEPRO.2022.132244.
[16] M.S. Sivakami, T. Gomathi, J. Venkatesan, H.S. Jeong, S.K. Kim, P.N. Sudha, Preparation and characterization of nano chitosan for treatment wastewaters, Int. J. Biol. Macromol. 57 (2013) 204–212, https://doi.org/10.1016/J.IJBIOMAC.2013.03.005.
[17] N. Aramesh, A.R. Bagheri, M. Bilal, Chitosan-based hybrid materials for adsorptive removal of dyes and underlying interaction mechanisms, Int. J. Biol. Macromol. 183 (2021) 399–422, https://doi.org/10.1016/J.IJBIOMAC.2021.04.158.
[18] M. Zubair, M. Arshad, A. Ullah, Chitosan-based materials for water and wastewater treatment, Handb. Chitin Chitosan. (2020) 773–809, https://doi.org/10.1016/B978-0-12-8179 66-6.00025-X.
[19] S. He, J. Li, X. Cao, F. Xie, H. Yang, C. Wang, C. Bittencourt, W. Li, Regenerated cellulose/chitosan composite aerogel with highly efficient adsorption for anionic dyes, Int. J. Biol. Macromol. 244 (2023) 125067, https://doi.org/10.1016/J.IJBIOMAC.2023. 125067.
[20] P. Sapuła, K. Bialik-Wąs, K. Malarz, Are natural compounds a promising alternative to synthetic cross-linking agents in the preparation of hydrogels? Pharm 15 (2023) 253, https://doi.org/10.3390/PHARMACEUTICS15010253.
[21] E.D. de Freitas, B.M. Lima, P.C.P. Rosa, M.G.C. da Silva, M.G.A. Vieira, Evaluation of proanthocyanidin-crosslinked sericin/alginate blend for ketoprofen extended release, Adv. Powder Technol. 30 (2019) 1531–1543, https://doi.org/10.1016/J.APT. 2019.04.031.
[22] V.A.J. Silva, P.L. Andrade, M.P.C. Silva, A.D. Bustamante, L. De Los Santos Valladares, J. Albino Aguiar, Synthesis and characterization of Fe3O4 nanoparticles coated with fucan polysaccharides, J. Magn. Magn. Mater. 343 (2013) 138–143, https://doi.org/10.1016/J.JMMM.2013.04.062.
[23] Q. Zhang, Y. Zhang, Y. Li, P. Ding, S. Xu, J. Cao, Green synthesis of magnetite nanoparticle and its regulatory effect on fermentative hydrogen production from lignocellulosic hydrolysate by Klebsiella sp, Int. J. Hydrog. Energy 46 (2021) 20413–20424, https://doi.org/10.1016/J.IJHYDENE.2021.03.142.
[24] A.E.S. Pereira, P.M. Silva, J.L. Oliveira, H.C. Oliveira, L.F. Fraceto, Chitosan nanoparticles as carrier systems for the plant growth hormone gibberellic acid, Colloids Surf. B: Biointerfaces 150 (2017) 141–152, https://doi.org/10.1016/J.COL-SURFB.2016.11.027.
[25] P.M. Morais da Silva, N.G. Camparotto, T. de Figueiredo Neves, K.T. Grego Lira, V. R. Mastelaro, C. Siqueira Franco Picone, P. Prediger, Effective removal of basic dye onto sustainable chitosan beads: batch and fixed-bed column adsorption, beads stability and mechanism, Sustain. Chem. Pharm. 18 (2020) 100348, https://doi.org/10.1016/J.SCP.2020.100348.
[26] T. de Figueiredo Neves, N. Barticiotto Dalarme, P.M.M. da Silva, R. Landers, C. Siqueira Franco Picone, P. Prediger, Novel magnetic chitosan/quaternary ammonium salt graphene oxide composite applied to dye removal, J. Environ. Chem. Eng. 8 (2020) 103820, https://doi.org/10.1016/J.JECE.2020.103820.
[27] M. Appu, Z. Lian, D. Zhao, J. Huang, Biosynthesis of chitosan-coated iron oxide (Fe3O4) hybrid nanocomposites from leaf extracts of *Brassica oleracea* L. and study on their antibacterial potentials, 3 Biotech 11 (2021) 271, https://doi.org/10.1007/s13205-021-02820-w.
[28] V. Thamilarasan, V. Sethuraman, K. Gopinath, C. Balalakshmi, M. Govindarajan, R. A. Mothana, N.A. Siddiqui, J.M. Khaled, G. Benelli, Single step fabrication of chitosan nanocrystals using Penaeus semisulcatus: potential as new insecticides, antimicrobials and plant growth promoters, J. Clust. Sci. 29 (2018) 375–384, https://doi.org/10.1007/S10876-018-1342-1/FIGURES/9.
[29] E. Alehosseini, S. Tabarestani, H. Kharazmi, E. Alehosseini, H.S. Tabarestani, M. S. Kharazmi, S.M. Jafari, Physicochemical, thermal, and morphological properties of chitosan nanoparticles produced by ionic gelation, Foods 11 (2022) 3841, https://doi.org/10.3390/FOODS11233841.
[30] T. Biswas, S. Sana, S. Kubra, S. Awasthi, Green synthesis, characterization of iron-based nanofertilizer for sustainable release, and efficient use of nutrients of iron nanoparticles using green tea extract, Bionanoscience (2024) 581–593, https://doi.org/10.1007/s12668-023-01204-z.
[31] Y. Cheng, A. Li, W. Shi, L. Zhao, Magnetic chitosan-functionalized waste carton biochar composites for efficient adsorption of anionic and cationic dyes, Chem. Eng. J. 481 (2024) 148535, https://doi.org/10.1016/J.CEJ.2024.148535.
[32] A. Alishahi, A. Mirvaghefi, M.R. Tehrani, H. Farahmand, S. Koshio, F.A. Dorkoosh, M.Z. Elsabee, Chitosan nanoparticle to carry vitamin C through the gastrointestinal tract and induce the non-specific immunity system of rainbow trout (Oncorhynchus mykiss), Carbohydr. Polym. 86 (2011) 142–146, https://doi.org/10.1016/J.CARBPOL.2011. 04.028.
[33] K. Yu, J. Ho, E. McCandlish, B. Buckley, R. Patel, Z. Li, N.C. Shapley, Copper ion adsorption by chitosan nanoparticles and alginate microparticles for water purifica- tion applications, Colloids Surfaces A Physicochem. Eng. Asp. 425 (2013) 31–41, https://doi.org/10.1016/j.colsurfa.2012.12.043.
[34] M.E. Peralta, R. Nisticò, F. Franzoso, G. Magnacca, L. Fernandez, M.E. Parolo, E. G. León, L. Carlos, Highly efficient removal of heavy metals from waters by magnetic chitosan-based composite, Adsorption 25 (2019) 1337–1347, https://doi.org/10.1007/s10450-019-00096-4.
[35] S.A. Munim, M.T. Saddique, Z.A. Raza, M.I. Majeed, Fabrication of cellulose-mediated chitosan adsorbent beads and their surface chemical characterization, Polym. Bull. 77 (2020) 183–196, https://doi.org/10.1007/s00289-019-02711-4.
[36] K. Yang, H. Peng, Y. Wen, N. Li, Re-examination of characteristic FTIR spectrum of secondary layer in bilayer oleic acid-coated Fe3O4 nanoparticles, Appl. Surf. Sci. 256 (2010) 3093–3097, https://doi.org/10.1016/j.apsusc.2009.11.079.
[37] C. García, G. Montero, M.A. Coronado, B. Valdez, M. Stoytcheva, N. Rosas, R. Torres, C.A. Sagaste, Valorization of eucalyptus leaves by essential oil extraction as an added value product in Mexico, Waste Biomass Valoriz. 8 (2017) 1187–1197, https://doi.org/10.1007/s12649-016-9695-x.
[38] C. Yong, X. Chen, Q. Xiang, Q. Li, X. Xing, Recyclable magnetite-silver heterodimer nanocomposites with durable antibacterial performance, Bioact. Mater. 3 (2018) 80–86, https://doi.org/10.1016/J.BIOACTMAT.2017.05.008.
[39] R. Gupta, K. Pancholi, R. De Sa, D. Murray, D. Huo, G. Droubi, M. White, J. Njuguna, Effect of oleic acid coating of iron oxide nanoparticles on properties of magnetic polyamide-6 nanocomposite, JOM 71 (2019) 3119–3128, https://doi.org/10.1007/s11837-019-03622-5.
[40] P. Karpagavinayagam, C. Vedhi, Green synthesis of iron oxide nanoparticles using Avicennia marina flower extract, Vacuum 160 (2019) 286–292, https://doi.org/10.1016/J.VACUUM.2018.11.043.
[41] M.F. Queiroz, K.R.T. Melo, D.A. Sabry, G.L. Sassaki, H.A.O. Rocha, Does the use of chitosan contribute to oxalate kidney stone formation? Mar. Drugs 13 (2015) 141, https://doi.org/10.3390/MD13010141.
[42] M.G. Pineda, S. Torres, L.V. López, F.J. Enríquez-Medrano, R.D. De León, S. Fernández, H. Saade, R.G. López, Chitosan-coated magnetic nanoparticles prepared in one-step by precipitation in a high-aqueous phase content reverse microemulsion, Mol 19 (2014) 9273–9287, https://doi.org/10.3390/MOLECULES19079273.
[43] C.M. Patel, A.A. Barot, V. Kumar Sinha, Sequential liquefaction of Nicotiana tabacum stems biomass by crude polyhydric alcohols for the production of polyols and rigid polyurethane foams, J. Appl. Polym. Sci. 133 (2016), https://doi.org/10.1002/app.43974.
[44] R. Laus, T.G. Costa, B. Szpoganicz, V.T. Fávere, Adsorption and desorption of Cu (II), Cd(II) and Pb(II) ions using chitosan crosslinked with epichlorohydrin-triphosphate as the adsorbent, J. Hazard. Mater. 183 (2010) 233–241, https://doi.org/10.1016/j.jhazmat.2010.07.016.
[45] G. Martínez-Mejía, N.A. Vázquez-Torres, A. Castell-Rodríguez, J.M. del Río, M. Corea, R. Jiménez-Juárez, Synthesis of new chitosan-glutaraldehyde scaffolds

for tissue engineering using Schiff reactions, Colloids Surfaces A Physicochem. Eng. Asp. 579 (2019) 123658, https://doi.org/10.1016/J.COLSURFA.2019.123658.
[46] F. Doustdar, A. Olad, M. Ghorbani, Effect of glutaraldehyde and calcium chloride as different crosslinking agents on the characteristics of chitosan/cellulose nanocrystals scaffold, Int. J. Biol. Macromol. 208 (2022) 912–924, https://doi.org/10.1016/J.IJBIOMAC.2022.03.193.
[47] A.R. Karimi, B. Rostaminejad, L. Rahimi, A. Khodadadi, H. Khanmohammadi, A. Shahriari, Chitosan hydrogels cross-linked with tris(2-(2-formylphenoxy)ethyl) amine: swelling and drug delivery, Int. J. Biol. Macromol. 118 (2018) 1863–1870, https://doi.org/10.1016/J.IJBIOMAC.2018.07.037.
[48] J. Huang, Y. Liu, Y. Muhammad, J.Q. Li, Y. Ye, J. Li, Z. Li, R. Pei, Effect of glutaraldehyde-chitosan crosslinked graphene oxide on high temperature properties of SBS modified asphalt, Constr. Build. Mater. 357 (2022) 129387, https://doi.org/10.1016/J.CONBUILDMAT.2022.129387.
[49] S. Lotfi, F. Ghaderi, A. Bahari, S. Mahjoub, Preparation and characterization of magnetite–chitosan nanoparticles and evaluation of their cytotoxicity effects on MCF7 and fibroblast cells, J. Supercond. Nov. Magn. 30 (2017) 3431–3438, https://doi.org/10.1007/s10948-017-4094-5.
[50] D. Zhang, L. Jiang, J. Zong, S. Chen, C. Ma, H. Li, Incorporated α-amylase and starch in an edible chitosan–procyanidin complex film increased the release amount of procyanidins, RSC Adv. 7 (2017) 56771–56778, https://doi.org/10.1039/C7RA11142H.
[51] F. Bi, X. Zhang, R. Bai, Y. Liu, J. Liu, J. Liu, Preparation and characterization of antioxidant and antimicrobial packaging films based on chitosan and proanthocyanidins, Int. J. Biol. Macromol. 134 (2019) 11–19, https://doi.org/10.1016/J.IJBIOMAC.2019.05.042.
[52] M.P. Seah, The quantitative analysis of surfaces by XPS: a review, Surf. Interface Anal. 2 (1980) 222–239, https://doi.org/10.1002/sia.740020607.
[53] J.W. Pinder, G.H. Major, D.R. Baer, J. Terry, J.E. Whitten, J. Čechal, J.D. Crossman, A.J. Lizarbe, S. Jafari, C.D. Easton, J. Baltrusaitis, M.A. van Spronsen, M.R. Linford, Avoiding common errors in X-ray photoelectron spectroscopy data collection and analysis, and properly reporting instrument parameters, Appl. Surf. Sci. Adv. 19 (2024) 100534, https://doi.org/10.1016/j.apsadv.2023.100534.
[54] A. da S.V. de Almeida, V.R. Mastelaro, M.G.C. da Silva, P. Prediger, M.G.A. Vieira, Adsorption of 17α-ethinylestradiol onto a novel nanocomposite based on graphene oxide, magnetic chitosan and organoclay (GO/mCS/OC): kinetics, equilibrium, thermodynamics and selectivity studies, J. Water Process Eng. 47 (2022) 102729, https://doi.org/10.1016/J.JWPE.2022.102729.
[55] P.C. Li, G.M. Liao, S.R. Kumar, C.M. Shih, C.C. Yang, D.M. Wang, S.J. Lue, Fabrication and characterization of chitosan nanoparticle-incorporated quaternized poly(vinyl alcohol) composite membranes as solid electrolytes for direct methanol alkaline fuel cells, Electrochim. Acta 187 (2016) 616–628, https://doi.org/10.1016/J.ELECTACTA.2015.11.117.
[56] S. Rodrigues, A.M.R. da Costa, A. Grenha, Chitosan/carrageenan nanoparticles: effect of cross-linking with tripolyphosphate and charge ratios, Carbohydr. Polym. 89 (2012) 282–289, https://doi.org/10.1016/j.carbpol.2012.03.010.
[57] H.J. Kim, I.-S. Bae, S.-J. Cho, J.-H. Boo, B.-C. Lee, J. Heo, I. Chung, B. Hong, Synthesis and characteristics of NH2-functionalized polymer films to align and immobilize DNA molecules, Nanoscale Res. Lett. 7 (2012) 30, https://doi.org/10.1186/1556-276X-7-30.
[58] M. Kehrer, J. Duchoslav, A. Hinterreiter, M. Cobet, A. Mehic, T. Stehrer, D. Stifter, XPS investigation on the reactivity of surface imine groups with TFAA, Plasma Process. Polym. 16 (2019), https://doi.org/10.1002/ppap.201800160.
[59] Y. Yi, G. Tu, P.E. Tsang, S. Xiao, Z. Fang, Green synthesis of iron-based nanoparticles from extracts of Nephrolepis auriculata and applications for Cr(VI) removal, Mater. Lett. 234 (2019) 388–391, https://doi.org/10.1016/J.MATLET.2018.09.137.
[60] B. Desalegn, M. Megharaj, Z. Chen, R. Naidu, Green synthesis of zero valent iron nanoparticle using mango peel extract and surface characterization using XPS and GC-MS, Heliyon 5 (2019) e01750, https://doi.org/10.1016/J.HELIYON.2019.E01750.
[61] C. Liu, H. Liu, K. Zhang, M. Dou, B. Pan, X. He, C. Lu, Partly reduced graphene oxide aerogels induced by proanthocyanidins for efficient dye removal, Bioresour. Technol. 282 (2019) 148–155, https://doi.org/10.1016/j.biortech.2019.03.012.
[62] T. de F. Neves, N.G. Camparotto, E.A. Rodrigues, V.R. Mastelaro, R.F. Dantas, P. Prediger, New graphene oxide-safranin modified@polyacrylonitrile membranes for removal of emerging contaminants: the role of chemical and morphological features, Chem. Eng. J. 446 (2022) 137176, https://doi.org/10.1016/J.CEJ.2022.137176.
[63] A. Deepatana, M. Valix, Steric hindrance effect on adsorption of metal–organic complexes onto aminophosphonate chelating resin, Desalination 218 (2008) 297–303, https://doi.org/10.1016/j.desal.2007.02.025.
[64] T. de F. Neves, N.G. Camparotto, G. de V. Brião, V.R. Mastelaro, R.F. Dantas, M.G. A. Vieira, P. Prediger, Graphene oxide-safranin modified@polyacrylonitrile membranes for water purification: reuse and mechanism based on theoretical calculations and XPS analysis, J. Water Process Eng. 50 (2022) 103248, https://doi.org/10.1016/J.JWPE.2022.103248.
[65] M. Raeiszadeh, A. Hakimian, A. Shojaei, H. Molavi, Nanodiamond-filled chitosan as an efficient adsorbent for anionic dye removal from aqueous solutions, J. Environ. Chem. Eng. 6 (2018) 3283–3294, https://doi.org/10.1016/j.jece.2018.05.005.
[66] P.M.M. da Silva, N.G. Camparotto, T. Figueiredo Neves, V.R. Mastelaro, B. Nunes, C. Siqueira Franco Picone, P. Prediger, Instantaneous adsorption and synergic effect in simultaneous removal of complex dyes through nanocellulose/graphene oxide nanocomposites: batch, fixed-bed experiments and mechanism, Environ. Nanotech- nology, Monit. Manag. 16 (2021) 100584, https://doi.org/10.1016/j.enmm.2021.100584.
[67] Y. Hu, T. Guo, X. Ye, Q. Li, M. Guo, H. Liu, Z. Wu, Dye adsorption by resins: effect of ionic strength on hydrophobic and electrostatic interactions, Chem. Eng. J. 228 (2013) 392–397, https://doi.org/10.1016/j.cej.2013.04.116.
[68] M.E. Parolo, M.C. Savini, J.M. Vallés, M.T. Baschini, M.J. Avena, Tetracycline adsorption on montmorillonite: pH and ionic strength effects, Appl. Clay Sci. 40 (2008) 179–186, https://doi.org/10.1016/j.clay.2007.08.003.
[69] H. Molavi, A. Pourghaderi, A. Shojaei, Experimental study on the influence of initial pH, ionic strength, and temperature on the selective adsorption of dyes onto nanodiamonds, J. Chem. Eng. Data 64 (2019) 1508–1514, https://doi.org/10.1021/acs.jced. 8b01091.
[70] N.G. Camparotto, T. de F. Neves, G.M.P. Pereira, V.R. Mastelaro, P. Prediger, Synergistic effect in simultaneous adsorption of cationic and anionic emerging contaminants by chitosan aerogels containing nanocellulose-modified tannic acid, J. Water Process Eng. 53 (2023) 103749, https://doi.org/10.1016/J.JWPE.2023.103749.
[71] Ü. Ecer, A. Zengin, T. Şahan, Magnetic clay\zeolitic imidazole framework nanocomposite (ZIF-8@Fe3O4@BNT) for reactive orange 16 removal from liquid media, Colloids Surfaces A Physicochem. Eng. Asp. 630 (2021) 127558, https://doi.org/10.1016/J.COLSURFA.2021.127558.
[72] Chemicalize | ChemAxon, (n.d.). https://chemaxon.com/products/chemicalize (accessed April 19, 2022).
[73] M.X. Huo, Y.L. Jin, Z.F. Sun, F. Ren, L. Pei, P.G. Ren, Facile synthesis of chitosan-based acid-resistant composite films for efficient selective adsorption properties towards anionic dyes, Carbohydr. Polym. 254 (2021) 117473, https://doi.org/10.1016/J.CARBPOL.2020.117473.
[74] Y. Tao, P. Wu, Y. Dai, X. Luo, S. Manickam, D. Li, Y. Han, P. Loke Show, Bridge between mass transfer behavior and properties of bubbles under two-stage ultrasound-assisted physisorption of polyphenols using macroporous resin, Chem. Eng. J. 436 (2022) 135158, https://doi.org/10.1016/J.CEJ.2022.135158.
[75] A.S. Al-Wasidi, I.I.S. AlZahrani, H.I. Thawibaraka, A.M. Naglah, M.G. El-Desouky, M.A. El-Bindary, Adsorption studies of carbon dioxide and anionic dye on green adsorbent, J. Mol. Struct. 1250 (2022) 131736, https://doi.org/10.1016/J.MOLSTRUC.2021.131736.
[76] R. Gajera, R.V. Patel, A. Yadav, P.K. Labhasetwar, Adsorption of cationic and anionic dyes on photocatalytic flyash/TiO2 modified chitosan biopolymer composite, J. Water Process Eng. 49 (2022) 102993, https://doi.org/10.1016/J.JWPE.2022.102993.
[77] S. Salamat, M. Hadavifar, H. Rezaei, Preparation of nanochitosan-STP from shrimp shell and its application in removing of malachite green from aqueous solutions, J. Environ. Chem. Eng. 7 (2019) 103328, https://doi.org/10.1016/J.JECE.2019.103328.
[78] S. Ilhan, C.F. Iscen, N. Caner, I. Kiran, Biosorption potential of dried Penicillium restrictum for reactive Orange 122: isotherm, kinetic and thermodynamic studies, J. Chem. Technol. Biotechnol. 83 (2008) 569–575, https://doi.org/10.1002/JCTB.1836.
[79] S. Archin, S.H. Sharifi, G. Asadpour, Optimization and modeling of simultaneous ultrasound-assisted adsorption of binary dyes using activated carbon from tobacco residues: response surface methodology, J. Clean. Prod. 239 (2019) 118136, https://doi.org/10.1016/j.jclepro.2019.118136.
[80] J.T. Martins, C.H. Guimarães, P.M. Silva, R.L. Oliveira, P. Prediger, Enhanced removal of basic dye using carbon nitride/graphene oxide nanocomposites as adsorbents: high performance, recycling, and mechanism, Environ. Sci. Pollut. Res. (2020) 1–20, https://doi.org/10.1007/s11356-020-10779-z.
[81] S. Lagergren, Zur Theorie der Sogenannten Adsorption Gelöster Stoffe, Kungliga Svenska Vetenskapsakademiens, Handlingar. 24 (1898) 139.
[82] Y.S. Ho, G. McKay, Pseudo-second order model for sorption processes, Process Biochem. 34 (1999) 451–465, https://doi.org/10.1016/S0032-9592(98)00112-5.
[83] T. Wang, M. Jiang, X. Yu, N. Niu, L. Chen, Application of lignin adsorbent in wastewater treatment: a review, Sep. Purif. Technol. 302 (2022) 122116, https://doi.org/10.1016/j.seppur.2022.122116.
[84] K. Jedynak, B. Szczepanik, N.R. Edzia, P. Słomkiewicz, A. Kolbus, P. Rogala, Ordered Mesoporous Carbons for Adsorption of Paracetamol and Non-steroidal Anti-inflammatory Drugs: Ibuprofen and Naproxen from Aqueous Solutions, 2019, https://doi.org/10.3390/w11051099.
[85] F. Hosseini, S. Sadighian, H. Hosseini-Monfared, N.M. Mahmoodi, Dye removal and kinetics of adsorption by magnetic chitosan nanoparticles, Desalin. Water Treat. 57 (2016) 24378–24386, https://doi.org/10.1080/19443994.2016.1143879.
[86] S.E. Selim, G.A. Meligi, A.E. Abdelhamid, M.A. Mabrouk, A.I. Hussain, Novel composite films based on acrylic fibers waste/nano-chitosan for Congo red adsorption, J. Polym. Environ. 30 (2022) 2642–2657, https://doi.org/10.1007/s10924-022-02378-5.
[87] C.H. Giles, A.P. D'Silva, I.A. Easton, A general treatment and classification of the solute adsorption isotherm part. II. Experimental interpretation, J. Colloid Interface Sci. 47 (1974) 766–778, https://doi.org/10.1016/0021-9797(74)90253-7.
[88] E. Koutsopoulou, I. Koutselas, G.E. Christidis, A. Papagiannopoulos, I. Marantos, Effect of layer charge and charge distribution on the formation of chitosan - smectite bionanocomposites, Appl. Clay Sci. 190 (2020) 105583, https://doi.org/10.1016/J.CLAY.2020.105583.
[89] M. Sadeghi, M. Moradian, H.A. Tayebi, A. Mirabi, Removal of penicillin G from aqueous medium by PPI@SBA-15/ZIF-8 super adsorbent: adsorption isotherm, thermodynamic, and kinetic studies, Chemosphere 311 (2023) 136887, https://doi.org/10.1016/J.CHEMOSPHERE.2022.136887.

[90] O.M. Adedeji, K. Jahan, Removal of pollutants from aqueous product of Co-hydrothermal liquefaction: adsorption and isotherm studies, Chemosphere 321 (2023) 138165, https://doi.org/10.1016/J.CHEMOSPHERE.2023.138165.
[91] N. Sakkayawong, P. Thiravetyan, W. Nakbanpote, Adsorption mechanism of synthetic reactive dye wastewater by chitosan, J. Colloid Interface Sci. 286 (2005) 36–42, https://doi.org/10.1016/j.jcis.2005.01.020.
[92] P. Baskaralingam, M. Pulikesi, V. Ramamurthi, S. Sivanesan, Modified hectorites and adsorption studies of a reactive dye, Appl. Clay Sci. 37 (2007) 207–214, https://doi.org/10.1016/J.CLAY.2007.01.014.
[93] H.F. Nour, T. El Malah, E.K. Radwan, R.E. Abdel Mageid, T.A. Khattab, M.A. Olson, Main-chain donor-acceptor polyhydrazone mediated adsorption of an anionic dye from contaminated water, React. Funct. Polym. 158 (2021) 104795, https://doi.org/10.1016/J.REACTFUNCTPOLYM.2020.104795.
[94] S. Tunali, A. Ozcan, A. Ozcan, T. Gedikbey, Kinetics and equilibrium studies for the adsorption of Acid Red 57 from aqueous solutions onto calcined-alunite, J. Hazard. Mater. 135 (2006) 141–148, https://doi.org/10.1016/j.jhazmat.2005.11.033.
[95] N. Mansouriieh, M.R. Sohrabi, M. Khosravi, Adsorption kinetics and thermodynamics of organophosphorus profenofos pesticide onto Fe/Ni bimetallic nanoparticles, Int. J. Environ. Sci. Technol. 13 (2016) 1393–1404, https://doi.org/10.1007/S13762-016-0960-0/TABLES/3.
[96] R. Lafi, L. Abdellaoui, I. Montasser, W. Mabrouk, A. Hafiane, The effect of head group of surfactant on the adsorption of methyl red onto modified coffee residues, J. Mol. Struct. 1249 (2022) 131527, https://doi.org/10.1016/J.MOLSTRUC.2021.131527.
[97] A.S. Asranudin, D. Purnomo, H. Prasetyoko, Holilah Bahruji, Single-step synthesis and modification of CTAB-hectorite for efficient adsorption of methyl orange dye, Mater. Chem. Phys. 291 (2022) 126749, https://doi.org/10.1016/J.MATCHEMPHYS.2022.126749.
[98] S.B. Jadhav, S.N. Surwase, D.C. Kalyani, R.G. Gurav, J.P. Jadhav, Biodecolorization of azo dye remazol orange by Pseudomonas aeruginosa BCH and toxicity (oxidative stress) reduction in Allium cepa root cells, Appl. Biochem. Biotechnol. 168 (2012) 1319–1334, https://doi.org/10.1007/s12010-012-9860-z.